Department of Physics and Astronomy
University of Heidelberg

Bachelor Thesis in Physics
submitted by

Katja Schwarz

born in Mannheim (Germany)

2016

Spatio-Temporal Measurements of Water-Wave Height and Slope using Laser-Induced Fluorescence and Splines

This Bachelor Thesis has been carried out by Katja Schwarz at the
Institute of Environmental Physics (IUP) in Heidelberg
under the supervision of
Prof. Bernd Jähne

Abstract. Within the framework of this thesis an algorithm was designed, which extracts the height of water waves from a time series of along-wind surface profile images. The surface position is detected with help of thresholding and subsequently fitted on the basis of two-dimensional smooth spline fitting. As result a function of the height in space and time direction and its slope as well as its time derivative are obtained. For wind speeds of up to 10 m/s it was possible to identify the height with an accuracy of approximately 18 μm. Furthermore, a script for data evaluation was written, which computes general properties of the wave field, like the significant wave height and the mean square slope in along-wind direction, as well as the frequency spectra and the dispersion relation. Both tools were used to evaluate measurements with wind speeds from 2.5 m/s to 14 m/s performed at the Large Marseille-Luminy Wind-Wave Facility within the ASIST-campaign in June 2016. The wave field differs from pure wind waves to additional mechanically generated waves with frequencies of 0.9 Hz and 1.3 Hz.

Zusammenfassung. Im Rahmen dieser Arbeit wurde ein Algorithmus entworfen, der die Höhe von Wasserwellen aus einer Zeitserie von Aufnahmen des Wellenprofils in Windrichtung bestimmt. Die Position der Wasseroberfläche wird mit Hilfe eines Schwellenwertverfahrens detektiert und anschließend auf der Basis von zwei-dimensionalen glättenden Splines gefittet. Als Ergebnis erhält man eine Funktion der Höhe in Orts- und Zeitrichtung und deren Neigung sowie deren zeitlichen Ableitung. Für Windgeschwindigkeiten von bis zu 10 m/s war es möglich die Höhe mit einer Genauigkeit von etwa 18 μm zu bestimmen. Des Weiteren wurde ein Skript zur Datenauswertung geschrieben, das sowohl allgemeine Eigenschaften des Wellenfeldes, wie die signifikante Wellenhöhe und die mittlere quadratische Neigung in Windrichtung, als auch die Frequenzspektren und die Dispersionsrelation berechnet. Beide Methoden wurden verwendet, um Messungen mit Windgeschwindikeiten zwischen 2.5 m/s und 14 m/s auszuwerten, die an der Large Marseille-Luminy Wind-Wave Facility im Rahmen der ASIST-Kampagne im Juni 2016 durchgeführt wurden. Die Wellenfelder variieren zwischen ausschließlich Wind-generierten und zusätzlich mechanisch generierten Wellen mit Frequenzen von 0.9 Hz und 1.3 Hz.

Contents

1. Introduction

The world's oceans cover about 71% of the earth's surface and play a key role in the global carbon cycle. Besides acting as sink and source for atmospheric carbon dioxide they also provide its largest reservoir. As recent anthropogenic emissions of greenhouse gases like CO_2 are the highest in history [IPCC, 2014], their impact on the oceans is of great interest. Therefore, it is fundamental to understand the processes of air-sea interaction.

The gas exchange, i.e. the mass flux j between air and water, depends on the concentration difference Δc, as well as its efficiency, characterized by the transfer velocity k. The transfer velocity also depends on physico-chemical properties of the trace gas like the solubility and the diffusion constant. Furthermore, it is influenced by various complex processes near the surface, as shown in figure 1. One factor, that impacts the transfer velocity, are waves, i.e. the dynamics of the water surface. In order to

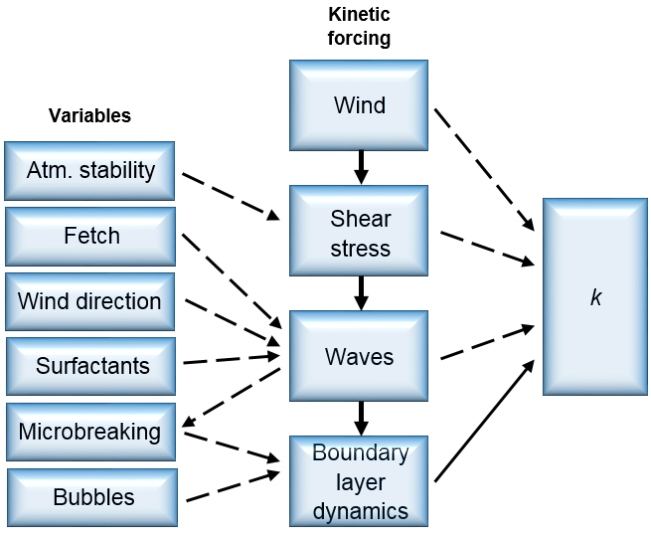

Figure 1: Simplified schematic of physical factors that influence the transfer velocity k. Through exchange of momentum, wind generates shear stress and waves, which in turn alter the boundary layer dynamics. The near-surface turbulence ultimately controls the transfer velocity. Furthermore, the properties of the wave field, and thus k, are affected by various environmental factors. Modified after Wanninkhof et al. [2009].

quantify the wave field, parameters like the significant wave height[1] and the mean square slope[2] have proven useful, as they are measures for the statistical distribution of the waves and the roughness of the water surface, respectively. Moreover, a spectral representation is extremely favorable, as it yields concentrated information about the characteristics of the wave field. All of this creates the need for a reliable detection of the position of the water surface.

Various techniques to measure the surface position and its shape have been developed over the past decades. A widely used approach is to measure the height with wave wires, which basically consist of two parallel conductors, see for example Chen [1994] or Peter [2015]. The underlying idea is, that the resistance of the conductors changes linearly with water depth. A major advantage of this method is the low expenditure. However, it is often desirable to use methods, which do not require direct contact with the water, as waves and wind might impact the setup. Here, techniques based on optical measurements provide an excellent alternative. Early attempts based on stereo photography go back more than a century. The height was then retrieved from the images by hand, see for instance Laas [1905]. Modern approaches use quantitative visualization techniques in combination with image processing. In 1992 Waas and Jähne developed a system for combined slope-height measurements, also based on the principle of stereopsis. In his work, Kiefhaber [2010] enhanced this system and introduced the *reflective stereo slope gauge* (RSSG), where light reflection is utilized to determine slope and height of the wave field. Another approach is based on the refraction of light and goes back to Jähne [1983]. It was modified by Balschbach [2000] and Rocholz [2008], who used a *color imaging slope gauge* (CISG), to determine the slope of the waves. Knowledge of the gradient of the wave field allows a subsequent reconstruction of the height.

Due to their great potential in accuracy, optical methods are still an active field of research. In 2013 Horn used laser-induced fluorescence to visualize the water surface at one point and extracted the height by subsequent image processing. The framework of this thesis is based on a similar approach, but in the meantime the laser point, used by Horn to detect the water surface, was extended to a laser sheet. Consequently, it is now possible to obtain spatio-temporal information about the wave field, enabling a two-dimensional description. For this purpose an algorithm, that extracts and fits the height from a series of images, was designed within this work. General properties of the wave field, like the significant wave height and the mean square slope in

[1] i.e. the mean height of the highest third of the waves

[2] defined as the sum of the variances of the slope components

along-wind direction, as well as height and slope frequency spectra and the dispersion relation are then reconstructed from the measured heights with a script developed in this thesis. The algorithm and the script for data evaluation were applied to data sets from a measurement campaign in Marseille (ASIST-campaign June 2016), where measurements for different wind speeds and under the influence of mechanically generated waves were made.

2. Theory

In the following sections the physical background (section 2.1) and some theoretical basics on image processing (section 2.2), that are used in this thesis, are provided.

2.1. Physical Background

The subsequent sections examine the physical background of deep water surface waves. It is assumed that the wave motion is unaffected by earth's rotation, i.e. that the wave frequency is much larger than the Coriolis frequency [Kundu and Cohen, 2008]. Furthermore amplitudes are considered to be small, such that the governing equations become linear. The general dispersion relation of small amplitude waves is derived in section 2.1.1. Special cases for gravity and capillary waves are presented in section 2.1.2, where the restoring force is dominated by gravity and surface tension, respectively. Lastly, in section 2.1.3 the energy density of the wave field is discussed, which also comprises a description of the power spectrum.

2.1.1. Small Amplitude Waves

The constraint to small amplitudes allows to linearize the governing equations, yielding an analytical solution to describe the waves. Oscillations at the free surface are considered small, when their amplitude a is small compared to the water depth H and the wavelength λ, i.e. $a/H \ll 1$ and $a/\lambda \ll 1$. The first condition justifies the evaluation of the velocity potential at $z = 0$ instead of $z = \eta$ because undisturbed and instantaneous water depth do not differ significantly. The second condition implies that the slope of the sea surface is small. Therefore, the free surface can be treated as a linear superposition of plane waves. Moreover, it is sufficient to make the following common assumptions:
We consider water to be an incompressible fluid

$$\nabla \mathbf{u} = 0 \tag{2.1}$$

where $\mathbf{u}$ denotes the fluid velocity. Due to small viscosity, viscous effects shall not affect wave propagation significantly. The flow is regarded as irrotational, which allows for the definition of a velocity potential Φ such that

$$\mathbf{u} = \nabla \Phi \ . \tag{2.2}$$

For a two-dimensional, steady flow the system is then described by Laplace's equation

$$\Delta \Phi = 0 \ . \tag{2.3}$$

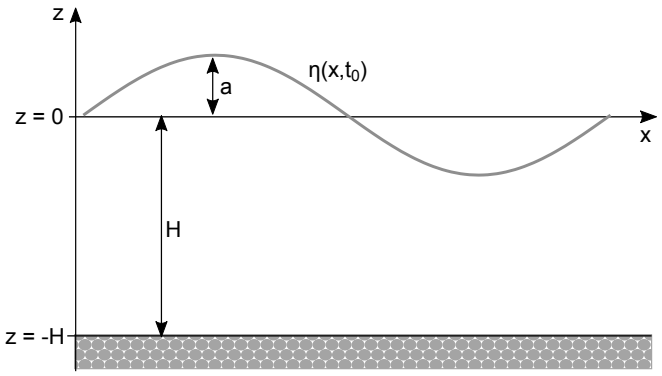

Figure 2: Coordinate system and wave nomenclature. Representation based on Kundu and Cohen [2008, chap. 7.4].

In the following the wave shall propagate in x-direction only. The free surface displacement $\eta(x,t)$ occurs in z-direction, where $z = 0$ denotes the position of the undisturbed surface. The coordinate axes are chosen accordingly to figure 2.
To solve Laplace's equation the formulation of boundary conditions is vital. The *kinematic boundary* states, that a fluid particle never leaves the surface

$$\frac{\partial \eta}{\partial t} + u \frac{\partial \eta}{\partial x}\bigg|_{z=\eta} = \frac{\partial \Phi}{\partial z}\bigg|_{z=\eta} \tag{2.4}$$

and that the normal velocity component vanishes at the bottom

$$\frac{\partial \Phi}{\partial z}\bigg|_{z=-H} = 0 \ . \tag{2.5}$$

For small amplitude waves both u and $\partial\eta/\partial x$ are small and as pointed out above, the right hand side can be evaluated at $z = 0$ instead of $z = \eta$. Therefore equation 2.4 simplifies to

$$\frac{\partial \eta}{\partial t} = \frac{\partial \Phi}{\partial z} \quad \text{at } z = 0 \ . \tag{2.6}$$

Additionally, ambient pressure and pressure just below the surface must be equal, which is reflected in the *dynamic boundary condition*

$$\frac{\partial \Phi}{\partial t} = \frac{\sigma}{\rho} \frac{\partial^2 \eta}{\partial x^2} - g\eta \quad \text{at } z = 0 \tag{2.7}$$

where the first term on the right hand side accounts for pressure change due to surface tension σ. The second term is subject to 'hydrostatic' pressure [Kundu and Cohen, 2008, chap. 7.7]. Consider an arbitrary disturbance of the free surface. By Fourier

analysis it can be decomposed into various sinusoidal components, which motivates the choice of the following ansatz for the surface elevation

$$\eta(x,t) = a\,\cos(kx - \omega t) \tag{2.8}$$

where a denotes the wave's amplitude, and k and ω are wavenumber and frequency, respectively. Substitution into Laplace's equation (equation 2.3) and using solely kinematic boundaries (equation 2.5 and 2.6) yields

$$\Phi = \frac{a\omega}{k}\frac{\cosh\,k(z+H)}{\sinh\,kH}\,\sin(kx-\omega t)\ . \tag{2.9}$$

From the dynamic boundary condition follows the *dispersion relation for small amplitude waves*

$$\omega = \sqrt{kg\left(1+\frac{\sigma}{\rho g}k^2\right)\tanh kH} \tag{2.10}$$

which can also be expressed in terms of the phase velocity $c = \omega/k$

$$c = \sqrt{\left(\frac{g}{k}+\frac{\sigma}{\rho}k\right)\tanh kH}\ . \tag{2.11}$$

2.1.2. Deep Water Gravity and Capillary Waves

From the previously derived relation between frequency ω and wavenumber k, gravity and surface tension can be identified as driving mechanisms of the restoring force. Depending on the wavelength either one or another factor prevails. Equilibrium in clean water at 20°C is obtained for waves with $\lambda = 2\pi\sqrt{\sigma/\rho g} = 1.7\,\text{cm}$. Then the phase speed becomes minimal [Phillips, 1977, chap. 3.2]. In the following the water is assumed to be deep, in the sense that $kH \gg 1$, i.e. $\tanh kH \approx 1$.
When $\lambda > 7\,\text{cm}$, effects of surface tension can be neglected, leading to *gravity waves* [Kundu and Cohen, 2008, chap. 7.4]. Then the dispersion relation (equation 2.10) simplifies to

$$\omega = \sqrt{kg} \quad \text{for} \quad \frac{\sigma}{\rho g}k^2 \ll 1 \quad \text{and} \quad kH \gg 1\ . \tag{2.12}$$

The complementary scenario of *capillary waves* is observed, when the restoring force is dominated by surface tension. For the dispersion relation follows from equation 2.10

$$\omega = \sqrt{\frac{\sigma}{\rho}k^3} \quad \text{for} \quad \frac{\sigma}{\rho g}k^2 \gg 1 \quad \text{and} \quad kH \gg 1\ . \tag{2.13}$$

2.1.3. Energy Density of the Wave Field

In linear wave theory the *total energy density* for deep water gravity waves is

$$E = \rho g \ \overline{\eta(\mathbf{x},t)^2} \tag{2.14}$$

and

$$E = \sigma \ \overline{(\nabla\eta(\mathbf{x},t))^2} = \sigma \ \overline{s(\mathbf{x},t)^2} \tag{2.15}$$

for deep water capillary waves with the slope s, respectively. The spectral energy density $X(\mathbf{k},\omega)$, can be calculated in terms of the Fourier transform of the surface displacement

$$X(\mathbf{k},\omega) = |\tilde{\eta}(\mathbf{k},\omega)|^2 \ . \tag{2.16}$$

This is also referred to as *power density spectrum*. Note, that by taking the squared absolute value any phase information is lost.
In particular it holds that

$$\int_{-\infty}^{+\infty}\int_{-\infty}^{+\infty} X(\mathbf{k},\omega)\mathrm{d}\mathbf{k}\ \mathrm{d}\omega = \overline{\eta^2} \ . \tag{2.17}$$

The *wavenumber (power density) spectrum* $\Psi(\mathbf{k})$ follows from integration over all frequencies ω

$$\Psi(\mathbf{k}) = \int_{-\infty}^{+\infty} X(\mathbf{k},\omega)\mathrm{d}\omega \ . \tag{2.18}$$

In the same manner the *frequency (power density) spectrum* $\phi(\omega)$ is obtained. However, for a statistically stationary wave field the frequency spectrum is real valued and symmetric about $\omega = 0$, which justifies the formulation

$$\phi(\omega) = 2 * \int_{-\infty}^{+\infty} X(\mathbf{k},\omega)\mathrm{d}\mathbf{k} \quad \text{for} \quad \omega \geq 0 \ . \tag{2.19}$$

These equations are for example derived in Phillips [1977, chap. 3.2 & chap. 4.1].

2.2. Image Processing

The following sections give an overview over basic techniques used to extract data from images. Starting with the impact of digitalization on a signal, section 2.2.1 introduces the *Sampling Theorem* and the effect of *aliasing*. Next, some basic operations on digital images are reviewed. The *Fourier transformation* is presented briefly in section 2.2.2, as it provides an essential tool in digital image processing, and the principle of *segmentation* is subject to section 2.2.3. The description of these concepts is based on Jähne [2012]. Furthermore, different types of *splines* are presented in section 2.2.4, as they are valuable instruments for data fitting.

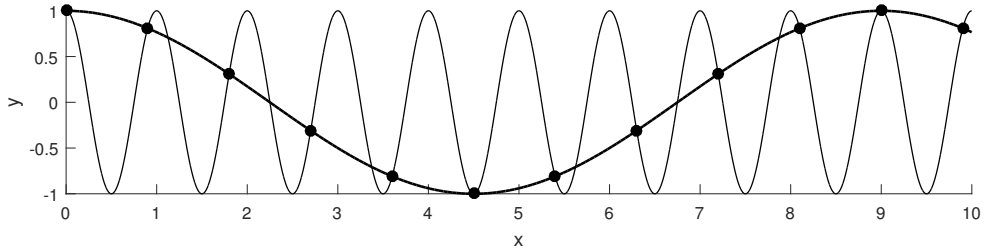

Figure 3: Visualization of the aliasing-effect: The periodic signal is sampled with 9/10 of the wavelength. This violates the Sampling Theorem and results in a distorted reconstructed signal. The reconstructed wavelength is nine times larger than the original wavelength. Representation based on Jähne [2012, chap. 5.1]).

2.2.1. Sampling

Typically, the sensor elements (*pixel*) are arranged on a rectangular grid. This motivates the interpretation of a monochrome image as two-dimensional array of gray values $g_{m,n}$, where m and n denote the pixel position on the grid. Let the sensor consist of $M \times N$ quadratic pixels of length Δx. Then, the field of view $X \cdot Y$ is specified by:

$$X = M\Delta x \tag{2.20}$$

$$Y = N\Delta x \ . \tag{2.21}$$

The limited size of the observed area generates a loss of information on scales larger than X and Y in the respective directions. Consequently, the original form of the underlying continuous signal cannot be reconstructed exactly anymore, if it exceeds the field of view. Similarly, the pixel size Δx determines a minimum scale, on which periodic structures of the signal can be observed. To predict the underlying signal correctly, at least two discrete sampling points per wavelength are needed, yielding

$$\lambda_{min} = 2\Delta x \ . \tag{2.22}$$

Equation 2.22 is also referred to as the *Sampling Theorem*. Its violation leads to signal distortion. An example is given in figure 3, where the reconstructed wavelength turns out much larger than the wavelength of the original signal. In case of a one-dimensional signal, this effect is called *aliasing*.

2.2.2. Fourier Transformation

Generally speaking, the Fourier transformation specifies the transition from position space to frequency space[3] and vice versa. It operates on the space of integrable functions[4]. The *continuous Fourier transformation* (FT) of a function $g(\mathbf{x})$ is given by:

$$\tilde{g}(\mathbf{k}) = \frac{1}{2\pi} \int_{-\infty}^{+\infty} g(\mathbf{x}) \, \exp(-2\pi \mathrm{i} \mathbf{k}^T \mathbf{x}) \mathrm{d}\mathbf{x} \tag{2.23}$$

with the inverse transformation

$$g(\mathbf{x}) = \int_{-\infty}^{+\infty} \tilde{g}(\mathbf{k}) \, \exp(2\pi \mathrm{i} \mathbf{k}^T \mathbf{x}) \mathrm{d}\mathbf{k} \ . \tag{2.24}$$

In data analysis usually discrete data points rather than continuous functions are subject of interest. Accordingly, it is beneficial to consider the one-dimensional *discrete Fourier transformation* (DFT), which maps complex valued vectors of length N to complex valued vectors of length N:

$$\tilde{g}_{\tilde{n}} = \frac{1}{N} \sum_{n=0}^{N-1} g_n \, \exp\left(-\frac{2\pi \mathrm{i} n \tilde{n}}{N}\right) \tag{2.25}$$

with the inverse transformation

$$g_n = \sum_{\tilde{n}=0}^{N-1} \tilde{g}_{\tilde{n}} \, \exp\left(\frac{2\pi \mathrm{i} n \tilde{n}}{N}\right) \ . \tag{2.26}$$

Note that real valued data is thereby interpreted as complex valued with vanishing imaginary part.

Additionally, two important properties of the Fourier transformation shall be mentioned, which are also discussed comprehensively in Jähne [2012, part III]. The *convolution theorem* indicates, that a convolution in position space corresponds to a multiplication in frequency space and vice versa:

$$h(\mathbf{x}) * g(\mathbf{x}) \quad \circ\!\!-\!\!\bullet \quad \tilde{h}(\mathbf{x}) \tilde{g}(\mathbf{x}) \ . \tag{2.27}$$

Furthermore, it holds that the partial derivative in position space is equivalent to a multiplication in frequency space:

$$\frac{\partial g(\mathbf{x})}{\partial x_d} \quad \circ\!\!-\!\!\bullet \quad 2\pi \mathrm{i} k_d \tilde{g}(\mathbf{k}) \ . \tag{2.28}$$

[3] i.e. Fourier space

[4] in the sense that for a function $g(\mathbf{x}) \ : \ \mathbb{R}^D \mapsto \mathbb{C}$

$$\int_{-\infty}^{+\infty} |g(\mathbf{x})|^2 \mathrm{d}\mathbf{x} < \infty$$

2.2.3. Segmentation

Image segmentation is typically used to identify and locate objects in digital images. In principle a binary image is created, by assigning the value one to pixels belonging to objects and zero to all others. This leads to a partition of the digital image into multiple regions, marking objects, boundaries and background.
The simplest approach to generate the binary image is by thresholding. Here, pixels with gray values above a certain threshold are assigned the value one, whereas all others are set to zero. The difficulty of this method lies in determining the optimal threshold value. A first impression can be gained by looking at the histogram of gray values. Usually this follows a bi-modal distribution, i.e. shows two peaks representing two classes of pixels (foreground pixels and background pixels). Then Otsu's method is an established way of finding the ideal threshold, where the term 'ideal' states, that the chosen value minimizes the variance in both pixel classes. For a more detailed description see Otsu [1979].

2.2.4. Splines

In general, a spline of degree q is constructed from piecewise polynomials of maximum degree q, such that the resulting function is $(n-1)$ times continuously differentiable. The points where neighboring pieces are joint are called *knots*. Additional to their smooth behavior at the knots, even high order splines do not struggle with oscillations at the interval edges, which is a common problem in polynomial interpolation. These advantageous properties make splines a fundamental tool for interpolation tasks, and, as for instance shown by Reinsch [1967] in his work on smoothing splines, also extremely suitable for smooth data fitting. Within the framework of this thesis the special cases of the cubic smoothing spline discussed in De Boor [1978], as well as penalized, i.e. P-Splines introduced by Eilers and Marx [1996], are examined.

The Cubic Smoothing Spline The essential idea of smooth data fitting with splines is to add a penalty term to the least squares function. This proposal was already made by Whittaker [1923] and picked up again by Schoenberg [1964] as well as Reinsch [1967]. The latter suggest to choose the model function $f(x)$ with existing m-th derivative $f^{(m)}$ for a set of approximate data points y_i with variance δy_i, such that it minimizes:

$$S = p \sum_{i=1}^{N} \left(\frac{y_i - f(x_i)}{\delta y_i} \right)^2 + (1-p) \int_{x_1}^{x_N} \left(f^{(m)}(t) \right)^2 \mathrm{d}t \ . \tag{2.29}$$

Via the smoothing parameter $p \in [0,1]$ a compromise between staying close to the data points, and a smooth fit is realized. Note, that for $p = 0$ $f(x)$ becomes the least-squares straight-line fit to the data. Then again, choosing $p = 1$ yields the natural spline interpolant. Schoenberg [1964] showed, that the solution of equation 2.29 is a spline of order $\kappa = 2m$ with knots at $x_2, \ldots, x_N$ and natural boundary conditions $f^{(j)}(x_1) = f^{(j)}(x_N) = 0$, for $j = m, \ldots, \kappa - 2$. For the special case of cubic splines, i.e. splines of order $\kappa = 4$, equivalent to equation 2.29, a linear system of equations can be solved [De Boor, 1978]. For this purpose we define

$$\mathbf{a} := [a_1, \ldots, a_N]^T \qquad \text{with} \quad a_i := f(x_i) \tag{2.30}$$

$$\mathbf{c} := [c_2, \ldots, c_{N-1}]^T \qquad \text{with} \quad c_i := f^{(2)}(x_i)/2 \tag{2.31}$$

$$\mathbf{u} := \mathbf{c}/(3p) \ . \tag{2.32}$$

Further let $\mathbf{R}$ and $\mathbf{Q^T}$ be tridiagonal matrices of order $(N-2)$, and $(N-2) \times N$, respectively, with the general rows:

$$\mathbf{R}: \qquad \Delta x_{i-1},\ 2(\Delta x_{i-1} + \Delta x_i),\ \Delta x_i \tag{2.33}$$

$$\mathbf{Q^T}: \qquad \frac{1}{\Delta x_{i-1}},\ -\left(\frac{1}{\Delta x_{i-1}} + \frac{1}{\Delta x_i}\right),\ \frac{1}{\Delta x_i} \tag{2.34}$$

and let $\mathbf{D}$ denote the diagonal matrix containing the variances $\mathbf{D} = \mathrm{diag}(\delta y_1, \ldots, \delta y_N)$. Then, the solution of equation 2.29 can be obtained from:

$$\left(6(1-p)\mathbf{Q}^T\mathbf{D}^2\mathbf{Q} + p\mathbf{R}\right)\mathbf{u} = \mathbf{Q}^T\mathbf{y} \tag{2.35}$$

and

$$\mathbf{a} = \mathbf{y} - 6(1-p)\mathbf{D}^2\mathbf{Q}\mathbf{u} \ . \tag{2.36}$$

A thorough derivation of these equations can be found in De Boor [1978, chap. XIV].

P-Splines In 1996 Eilers and Marx modified the idea of the smoothing spline and introduced the *P-Spline*. An extension to higher dimensions by Eilers et al. followed in 2006. Below, the one- and two-dimensional cases are discussed.
The main difference to the smoothing spline lies in the idea to write the model function $f(x)$ in terms of a special set of basis functions, the B-Splines. A B-Spline of degree q is a function, that is composed of $q+1$ polynomial pieces, each of degree q. It is positive valued on a domain spanned by $q+2$ knots and zero everywhere else. Therefore, the basis functions (B-Splines) of the P-Spline, overlap (except at the boundaries) with $2q$ polynomial pieces of their neighbors. In figure 4 these properties are illustrated.

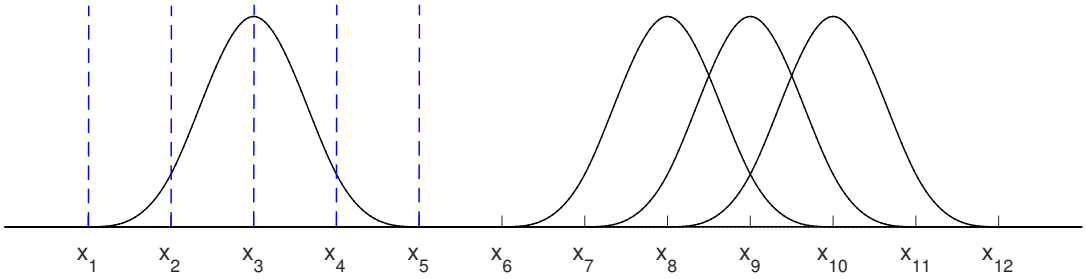

Figure 4: Illustration of B-Splines of degree $q = 3$. On the left an isolated B-Spline is shown. It consists of four polynomial pieces, that join at three inner knots (x_2 - x_4). The dashed lines indicate beginning and end of the pieces. On the right three overlapping B-Splines are pictured. The middle one overlaps with two polynomial pieces of each of its neighbors. Representation modified after Eilers and Marx [1996].

Likewise to all splines, their derivatives at the q inner knots are continuous up to order $q-1$. For further reading it is referred to De Boor [1978] and Eilers and Marx [1996]. Subsequently, we express the model function $f(x)$ as linear combination of parameters a_j in the B-Spline basis:

$$f(x) = \sum_{j=1}^{n} a_j B_j(x; q) \ . \tag{2.37}$$

Eilers and Marx point out, that it is sufficient to approximate the κ-th derivative with the finite differences operator Δ^κ of order κ. Similar to equation 2.29, the optimal fit minimizes the penalized least squares function, defined as

$$S = \sum_{i=1}^{m} (y_i - f(x))^2 + \lambda \sum_{j=\kappa+1}^{n} (\Delta^\kappa a_j)^2 \tag{2.38}$$

where λ denotes the smoothing parameter. Note, that in equation 2.38 the first term corresponds to common B-Spline regression and the second term approximates the smoothness penalty. Equivalent to minimizing equation 2.38 the set of penalized normal equations can be solved:

$$(\mathbf{B}^T\mathbf{B} + \lambda \mathbf{D}_\kappa^T \mathbf{D}_\kappa)\mathbf{a} = \mathbf{B}^T\mathbf{y} \tag{2.39}$$

with $\mathbf{D}_\kappa$ being the matrix representation of Δ^κ and $(\mathbf{B})_{ij} = B_j(x_i)$.
Let us now observe the two-dimensional case. Consider a set of M data points $y_m(v_i, x_j)$ on a grid of size $I \times J$. Let $\breve{\mathbf{B}}$, $I \times K$, and $\mathbf{B}$, $J \times L$, be the B-Spline

bases in v- and x-direction, respectively. Then, the model function $\xi(v, x)$ can be expressed in terms of the tensor product of the bases:

$$\xi(v,x) = \sum_{k=1}^{K}\sum_{l=1}^{L} \breve{B}_k(v) B_l(x) a_{kl} \tag{2.40}$$

where $\mathbf{A} = [a_{kl}]$ is the $K \times L$ coefficient matrix. For the subsequent steps it is beneficial to define an $M \times 1$ coefficient vector β, that contains the stacked columns of $\mathbf{A}$, i.e. $\beta = \mathrm{vec}(\mathbf{A})$. Use of the tensor product also yields the regression basis $\mathbf{C}$

$$\mathbf{C} = \mathbf{B} \otimes \breve{\mathbf{B}} \tag{2.41}$$

and the penalty matrices can be calculated from

$$\mathbf{P} = \mathbf{I}_K \otimes \mathbf{D}_\kappa^T \mathbf{D}_\kappa \tag{2.42}$$

$$\breve{\mathbf{P}} = \mathbf{I}_L \otimes \mathbf{D}_{\breve{\kappa}}^T \mathbf{D}_{\breve{\kappa}} \tag{2.43}$$

with $\mathbf{I_x}$ denoting the identity matrix of size x. The set of penalized normal equations can then be written as

$$(\mathbf{C}^T\mathbf{C} + \lambda\mathbf{P} + \breve{\lambda}\breve{\mathbf{P}})\beta = \mathbf{C}^T\mathbf{y} \ . \tag{2.44}$$

Note, that weights can be introduced by element-wise multiplication of $\mathbf{C}^T$ with a weight matrix $\mathbf{W}$. Thereby $\mathbf{W}$ is of size $M \times KL$ and repeats the weights for all data points in each column.

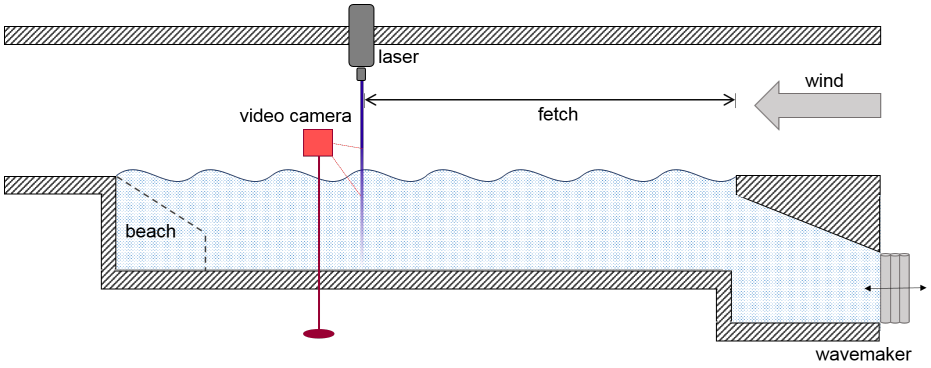

Figure 5: Schematic setup of the Large Marseille-Luminy Wind-Wave Facility. The water tank is 40 m long, 2.6 m wide and 0.9 m deep. The recirculating wind tunnel above is 3.2 m wide and 1.5 m high. The measurement section is located at a fetch of 28 m. Representation based on Caulliez [2013].

3. Setup

3.1. The Large Marseille-Luminy Wind-Wave Facility

The experimental data used in this thesis originates from a measurement campaign, carried out in June 2016 at the Large Marseille-Luminy Wind-Wave Facility of the Mediterranean Institute of Oceanography (MIO) in Marseille. A schematic set up of the wind-wave flume is depicted in figure 5. The facility comprises a 40 m long, 2.6 m wide and 0.9 m deep water tank[5] and a 3.2 m wide and 1.5 m high wind tunnel above. With air ducts above the tunnel, the air is recirculated from end to beginning, whereby steady wind speeds from 1 m/s - 14 m/s can be generated by an axial fan. A wavemaker is installed at the downwind end of the water tank and permits the creation of plane gravity waves at prescribed frequencies. Furthermore, a permeable wave absorber (beach) is set at the upwind end, in order to damp wave reflections. The measurement section sits at a fetch of 28 m and is equipped with glass windows, enabling optical access.

[5] More precisely, the depth of the tank increases linearly and starts at 0.7 m at the downwind end. At the measurement section the tank is 0.9 m deep.

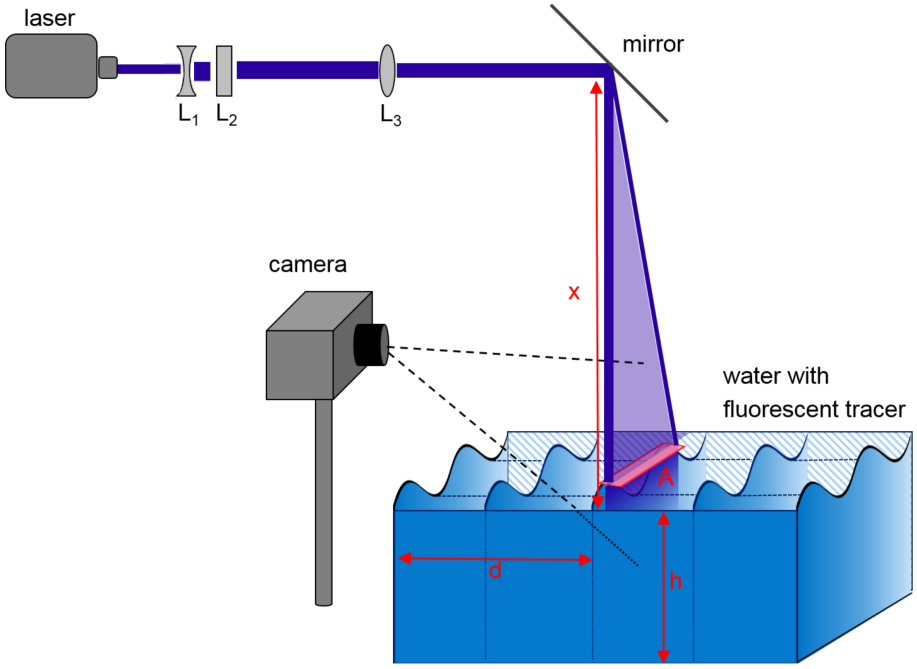

Figure 6: Sketch of the experimental setup. The surface profile is visualized with a laser sheet of size A = (30×2) mm, constructed by a configuration of different lenses (L_1-L_3). The distance to the side wall of the water tank amounts to d = 69 cm. The length of the beam is approximately x = 3 m and the water depth is h = 90 cm.

3.2. Experimental Setup

The experimental setup was designed in such a manner that it has no[6] impact on the observed wave field. For this purpose the height is processed from a series of gray scale images, which is recorded with a camera next to the wind-wave flume. Figure 6 shows a sketch of the installation. To obtain suitable images, a distinct gradient from water to air is vital. This is realized by adding the fluorescent indicator *Pyranine*[7] to the water. Pyranine is chosen due to its beneficial properties, like a large Stokes shift[8] of 61 nm, and high quantum efficiency, which means that nearly all absorbed light is emitted again. For further reading Kräuter [2015] is recommended. The surface profile

[6] Disregarding negligible heating of the surface and radiation pressure due to the laser.
[7] $C_{16}H_2Na_3O_{10}S_3$
[8] i.e. the difference between excitation and emission wavelength

is then visualized with a laser sheet of size A = (30 × 2) mm at a distance d = 69 cm from the side wall of the water tank (see figure 6). For construction, the laser beam is modified via three optical lenses [Raffel et al., 1998]. The configuration consists of two spherical (L_1, L_3) and one cylindrical lens (L_2), as shown in figure 7. The first lens has a negative focal length of −100 mm and consequently diverges the beam. The cylindrical lens is the essential element, as it only affects one dimension of the light beam. Therefore, its focal length (100 mm) mainly determines the along-wind length of the laser sheet (figure 7(a)). Lastly, a third lens (300 mm) is utilized to focus and control the thickness. The total length of the laser beam, before it hits the water, is approximately x = 3 m, and the laser itself consists of two combined 6 W laser diodes with a wavelength of $\lambda = 447$ nm. As camera a Basler acA1920-um155 camera was used with a Minolta 35 mm f/1.8 objective. For the measurements the maximum aperture was used and an interference filter was placed in front of the objective. The interference filter is used to dismiss any total reflections of the beam, which can for example arise from bubble formation. Moreover it guarantees, that solely wavelengths of the emission spectrum of Pyranine reach the camera sensor.

With the purpose of enabling a simple calibration, a special setup for the camera, shown in figure 8, was designed. Usually the CCD-sensor is positioned centered to the optical axis of the lens. Then the camera has to be tilted to observe the water surface, resulting in a complex calibration of the images. This method was previously used by Horn [2013] and Eisenhauer [2011]. Here, the sensor is shifted above the optical axis, allowing observations without tilting. Hence, the subsequent calibration simplifies to a scaling factor f_{cal}, which transforms the image size in pixel into the object size in meter. For the carried out experiments the scaling factor was determined with help of a chessboard patterned target and found to be $f_{cal} = 183\,\mu$m/pxl, meaning that a length of one pixel in the image corresponds to an observed length of 183 μm.

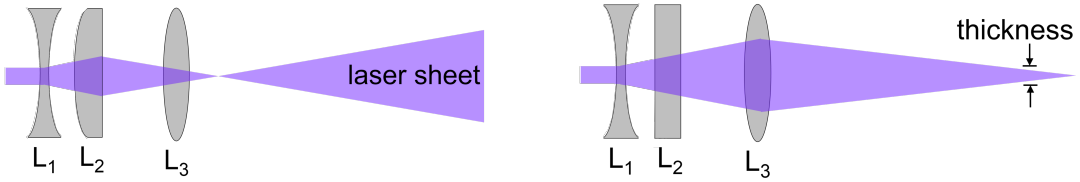

(a) Side view (b) Top view

Figure 7: Construction of a laser sheet with a configuration of two spherical (L_1, L_3) and one cylindrical lens (L_2). Representation based on Raffel et al. [1998].

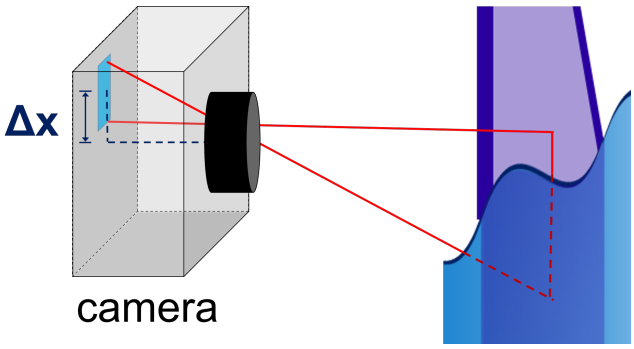

Figure 8: Sketch of the camera setup. Due to shifting the CCD-sensor (pictured as blue rectangle), the camera does not need to be tilted and a simple calibration becomes possible.

4. Experiments

The processed data originates from measurements at the Large Marseille-Luminy Wind-Wave Facility in Marseille (figure 5), performed from June 3 to 23, 2016 within the ASIST-campaign. Measurements were taken at wind speeds from 2.5 m/s - 14 m/s and the wavemaker was used to create paddle waves with frequencies of up to 1.3 Hz. Table 1 lists the conditions and an approximated total measurement time for all executed runs. With the set up described in section 3.2, image series were recorded with a frequency of 500 Hz. Additionally, a laser slope gauge (LSG) was installed at the same fetch and was used for simultaneous measurements of the slope. Moreover, the wave height was measured with wave wires 3 m behind the measurement section. To ensure that the wave field had reached equilibrium when measuring, the wind and wave generation was started at least 30 minutes prior to each run.

number of run	wind [m/s]	paddle [Hz]	duration [min]
1	2.5	-	30
2	3	-	30
3	4	-	30
4	5	-	10
5	6	-	45
6	6	0.9	30
7	6	1.1	25
8	6	1.3	30
9	8	-	90
10	8	0.9	40
11	10	-	40
12	10	0.9	35
13	10	1.3	30
14	12	-	30
15	12	0.9	40
16	14	-	40
17	14	0.9	17
18	14	1.3	40

Table 1: Conditions of all executed runs

5. Method

In the framework of this thesis it was aimed to design an algorithm which is capable of extracting the height of a water wave from a surface profile image. Therefore, the method presented by Horn [2013] was extended by one dimension, now based on a laser sheet instead of a one-dimensional laser point. The following sections explain the different procedures performed by the developed algorithm, which are also summarized and illustrated in figure 13. Section 5.1 focuses on extracting the height from the actual series of images, whereas section 5.2 deals with processing of the data and compares the implemented fitting mechanisms. In section 5.3 the course of action for data evaluation is explained. Lastly, calculation of the uncertainty is discussed in section 5.4.

5.1. Detection of the Water Surface

Due to laser-induced fluorescence (see section 3.2) the images show a bright wave profile, whereas the air on top appears dark. As already mentioned by Horn [2013], two major techniques exist to detect the water surface in such a grayscale image. The first method is the threshold method, previously discussed in section 2.2.3. Another approach is to examine the columnwise derivative of the gray values. Here, the underlying idea is that the change in gray values is maximal at the transition from foreground to background and vice versa. In the final version of the algorithm only thresholding was implemented, because the derivative method was found to be more prone to false detection. To extract the height from the time series of surface profile images the final version of the algorithm proceeds as follows.
Step 1: Determination of the Threshold Value: First of all a robust threshold value for each column of the grayscale images needs to be found. Therefore an image series corresponding to three seconds measurement time is read in, and ideal values are identified using Otsu's method (see section 2.2.3). Under the assumption, that the lighting conditions remain constant during a measurement series, the identified thresholds are representative for the complete series and thus are used for all images.
Since the intensity of the laser sheet lowers towards the edges, pixels in these regions can be darker and therefore yield less accurate results. For this reason, only columns with thresholds larger than 75 % of the maximum value are considered in the detection process. Lastly, a range of five threshold values is defined for each column, reaching from 90% to 110% of the detected threshold. Therefore, the height is detected for five slightly different threshold values, which enables a subpixel accurate computation of

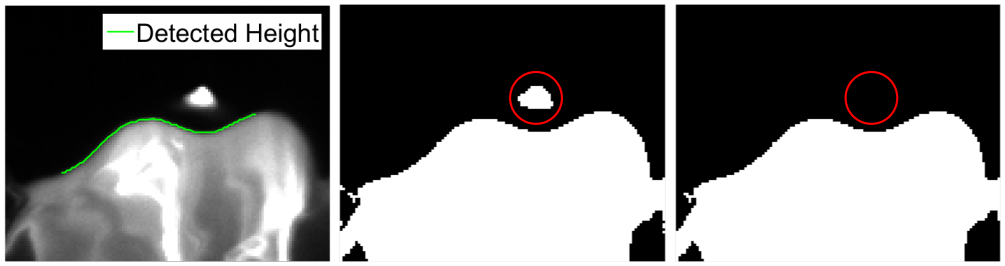

(a) Detected height (b) Before filtering (c) After filtering

Figure 9: Benefit of the object filter. In each binary image objects with less than 100 pixels are filtered. Therefore splashes and drops are discarded, so that the height is detected correctly at the water surface.

the surface position in the subsequent steps.
The following procedures are applied to every image of the complete time series:
Step 2: Image Segmentation: For each value of the threshold range the image is converted into a binary image. In order to discard splashes from wave breaking, all objects (i.e. pixel groups with value one) with less than 100 pixels are deleted. An example is shown in figure 9.

Step 3: Extract the Height: Next, the binary images are element-wise multiplied with a scaling matrix to obtain the surface position. The scaling matrix contains the mean height of each row in terms of pixel (see figure 13, step 3). Then, the surface position is simply given by the maximum value of each column of the product. Lastly, the height is obtained by averaging over the surface positions of all binary images within the threshold range.
To improve the accuracy, implausible heights are identified by their high standard deviation[9] and a local median filter is applied[10]. The values of these points are temporarily set to 'NaN' and subsequently reconstructed by interpolation (see section 5.2). Furthermore, images with less than 30% remaining data points are ignored completely, as such strong deviations indicate, that a reliable height detection was over all not possible in this image.

[9] Values with a standard deviation of more than 3 pxl were classified as implausible.
[10] Within a range of five neighboring columns the allowed maximum deviation from the median height was set to 8 pxl.

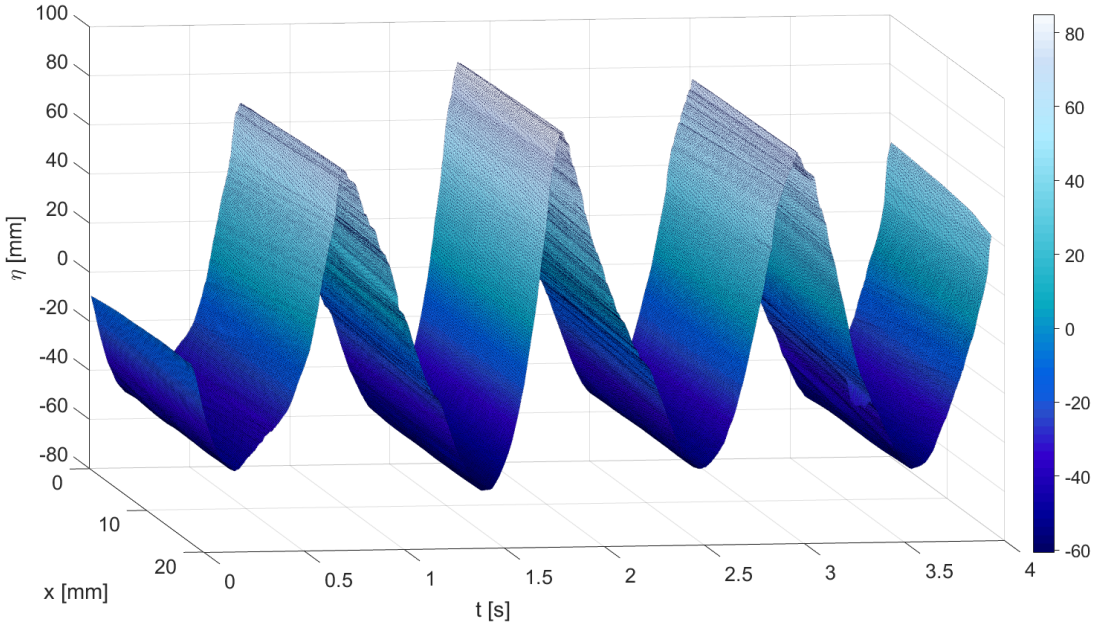

Figure 10: Excerpt of a spatio-temporal fit of the wave height at 10 m/s wind and mechanically generated waves with 0.9 Hz (run 12). The fit was carried out by the built-in MATLAB function for the cubic smoothing spline.

5.2. Data Processing

At this point, the extracted height in spatial direction is available for each image of the time series. Consequently, information is defined on a spatio-temporal surface. As continuous behavior of the waves is expected in both dimensions, a smooth course of the surface is motivated. The second part of the algorithm now concentrates on fitting this spatio-temporal information, with the splines presented in section 2.2.4. An example is given in figure 10. As result, the cubic smoothing spline as well as the P-Spline, i.e. penalized spline fit yield a continuous, two-dimensional function of the height. This allows to compute the derivatives analytically in time and space direction, instead of using finite difference schemes as an approximation. Consequently, continuous functions of the time derivative as well as the slope are obtained additional to the wave height.

In the following, the properties of the implemented spline methods are assessed. Firstly, theoretical pros and cons of each method are discussed. Then, their fitting properties are compared with respect to the data sets.

On the one hand, the two-dimensional P-Spline fit on the basis of Eilers et al. [2006]

was implemented. This method is very flexible and provides a wide range of adjustable parameters. Degree and order of the fit can be chosen separately for each dimension, and the respective total number of basis functions, i.e. B-Splines, can be adjusted. Moreover, it is possible to select a different smoothing parameter for each dimension. Hence, it is possible to vary the amount of smoothing among the dimensions. Furthermore, individual weights for every data point can be set (see section 2.2.4). This is a main advantage, because it allows to process values containing 'NaN's, as individual weights for these can be simply set to zero. Then again, the algorithm provided by Eilers et al. [2006] is only applicable to small to moderately sized surfaces. For this reason, the complete surface of data points has to be computed in segments which are subsequently patched together. To ensure a smooth transition between the patches, an overlap at the borders is initialized within the implemented fitting routine and values in this regions are averaged.

On the other hand a cubic smoothing spline via the built-in function "csaps" of MATLAB was utilized for data fitting. The cubic spline is less flexible than the penalized spline, as degree and order are set to the fixed values 3 and 2, respectively. Likewise to the P-Splines, the smoothing parameter can be chosen separately for each dimension, but weights can only be entered dimension-wise, permitting an individual weighting of data points. Therefore, the built-in MATLAB function of the cubic smoothing spline is not suitable to process data sets containing 'NaN's in more than one dimension. This is why in the implemented routine for the smoothing spline, these data points have to be interpolated preliminary to fitting. This process is time consuming, as it is computationally costly. Nevertheless, the smoothing spline remains competitive to the penalized spline, because it is capable of fitting large surfaces as a whole.

Next, we consider the performance of both methods on the actual data sets. For reasons of comparability, the P-Spline fit was executed with degree 3 and order 2, accordingly to degree and order of the cubic smoothing spline. The width of the surface patches for the penalized splines comprises the full detection range in x-direction, and 100 columns in t-direction, with an overlap of 10 columns between two surfaces. The number of basis functions, i.e. B-Splines, was set to $n_x = 20$ and $n_t = 50$. As the detection range usually comprised about 100 pixel, a B-Spline comprises approximately 5 pixel in space direction and 2 pixel in time direction and the smoothing parameters for the P-Spline fit were set to $\lambda_x = 0.01$ and $\lambda_t = 0.5$ in x- and t-direction, respectively. For the smoothing spline $p_x = 0.99$ and $p_t = 0.5$ were chosen. Therefore, both fits stick close to the spatially detected height and allow moderate smoothing in time direction.

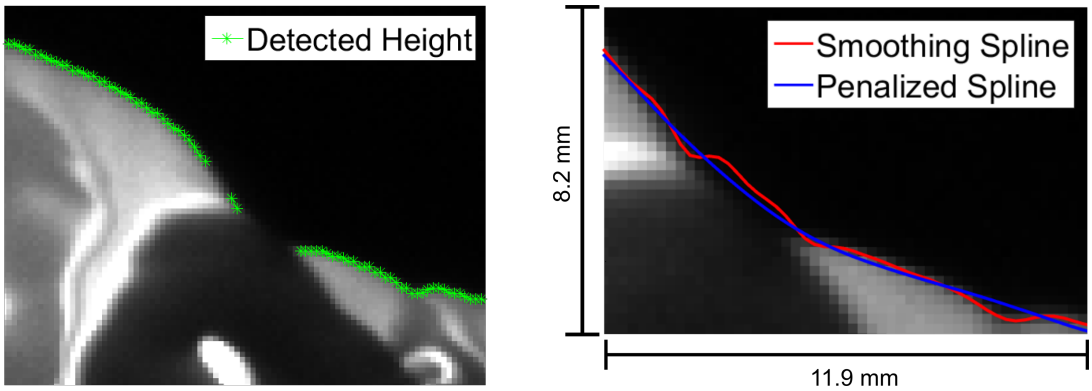

(a) Detected height

(b) Fitted height

Figure 11: Data interpolation with the implemented spline methods. As shown in (a), no height is detected at the dark region in the middle. The values are interpolated with splines, which is demonstrated in (b). Only on small scales differences in both methods become apparent. In figure (b) the difference between both fits was at most 0.29 mm. Over all, the P-Spline is found to provide a smoother fit, whereas the smoothing spline sticks closer to the detected height.

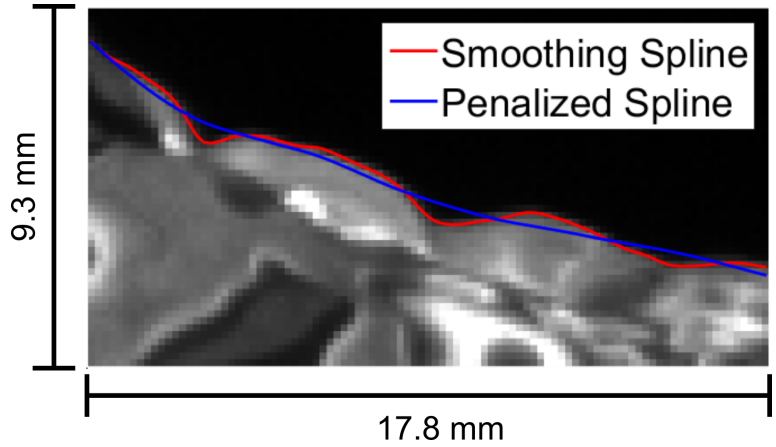

Figure 12: Over smooth fitting of the P-Spline. The basis functions (B-Splines) of the P-Spline comprise approximately 5 pixel (≈ 0.9 mm) in space direction and are of degree 3. Therefore, they are sometimes not flexible enough to capture small scale waves correctly.

In figure 11 the interpolation of data points is demonstrated. It can be seen, that the detected height of both methods differs on small scales, only. With the above settings, the P-Spline was found to provide smoother fitting than the cubic smoothing spline. This can be beneficial for the purpose of interpolation, as for instance shown in figure 11(b). Then again, it often leads to over smooth data fitting, resulting in a lack of ability to detect small wave lengths, which is depicted in figure 12. The cubic smoothing spline sticks closer to the data points, making it generally more sensitive to faulty detection, but also better in representing properly detected values. For this reason, the fits of the cubic smoothing spline were used to compute the wave spectra. Due to the statistics applied in the evaluation process, defective values are evened out, whereas a general loss of small wavelengths would create a grave deficit in information. The most important steps from the previous sections are again illustrated and summarized in figure 13, where an overview over the proceedings of the algorithm is given.

5.3. Data Evaluation

Additional to the height detection algorithm, a script for the purpose of data evaluation was written. It computes the frequency power spectra of height, slope, i.e. spatial derivative, and time derivative. Furthermore, the dispersion relation introduced in section 2.1.1 is calculated, and general wave properties, like maximum amplitude, significant wave height and mean square slope[11] of the wave field are determined. Moreover, the ratio of interpolated values to all values, i.e.

$$\epsilon = \frac{\#\text{'NaN'}}{\#\text{values}} \tag{5.45}$$

is evaluated. The script proceeds as follows.
For the frequency spectrum information is solely required in time direction and therefore a spectrum could be obtained for each position in spatial direction. However, as a precaution to correlation only every 20th column is treated as independent point of observation, which was considered sufficient, as the polynomial pieces comprise less than 5 pixel for the cubic smoothing spline. The height series at each point is then decomposed into smaller time sequences. Here, it is crucial to choose sufficiently long time segments, so all present wave lengths can occur several times within one sequence. Therefore, the length of a sequence was chosen to be one minute, which is satisfactory

[11] Here, only the mean square slope in along-wind direction is computed, as information is solely measured in one space dimension. Generally the mean square slope is defined as the sum of the variances in along- and cross-wind direction.

Figure 13: Illustration and brief summary of the procedures carried out by the developed algorithm.

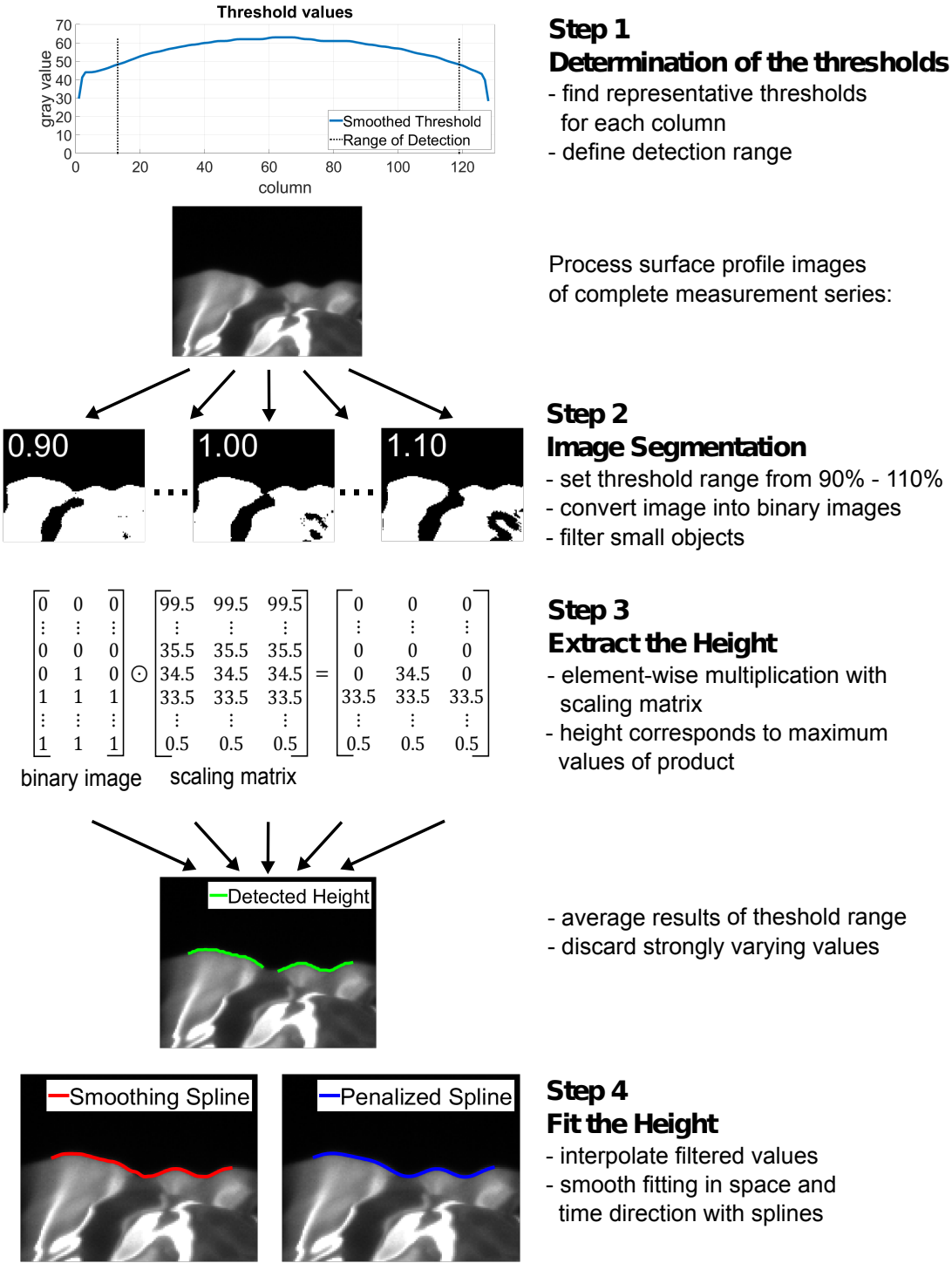

Step 1
Determination of the thresholds
- find representative thresholds for each column
- define detection range

Process surface profile images of complete measurement series:

Step 2
Image Segmentation
- set threshold range from 90% - 110%
- convert image into binary images
- filter small objects

Step 3
Extract the Height
- element-wise multiplication with scaling matrix
- height corresponds to maximum values of product

- average results of theshold range
- discard strongly varying values

Step 4
Fit the Height
- interpolate filtered values
- smooth fitting in space and time direction with splines

for the observed conditions. Next, frequency spectra of the sequences are computed individually. The final spectrum is then the ensemble average.
To compute the phase speed, a fundamental property of the Fourier transform is exploited. As equation 2.28 states, execution of the spatial derivative in real space is equivalent to a multiplication with the wavenumber k in Fourier space. Likewise, the time derivative corresponds to a multiplication with the frequency ω. Therefore, dividing the frequency spectrum of the time derivative $\phi_{\dot{\eta}}$ by the frequency spectrum of the spatial derivative ϕ_s yields the dispersion relation

$$c = \frac{\omega}{k} = \sqrt{\frac{\phi_{\dot{\eta}}}{\phi_s}} \ . \tag{5.46}$$

Note, that the spectra and not the Fourier transforms are divided here, which requires to take the square root.
Additionally, the maximum amplitude is determined for positive as well as for negative surface elevation with respect to the mean height. It is also computed as ensemble average of all sequences, to correct for the possibility of defective values, and its uncertainty follows from the uncertainty of the mean. Likewise, the significant wave height and the mean square slope are obtained. Traditionally, the significant wave height is defined as the mean height from crest to trough of the highest third of the waves, but nowadays it is usually calculated as four times the standard deviation of the surface elevation [Holthuijsen, 2007], namely

$$H_s = 4 \ \sigma_\eta \ . \tag{5.47}$$

The mean square slope in along-wind direction is given by the variance of the slope

$$mss = \sigma_s^2 \ . \tag{5.48}$$

5.4. Uncertainty Estimation

As described in section 5.1, the algorithm computes the standard deviation σ_{ij} of the detected height from the range of threshold values for each column j in each image i. The uncertainty of the height $\Delta\eta$ is given by the uncertainty of the mean, i.e. $(\Delta\eta)_{ij} = \sigma_{ij}/\sqrt{5}$, as the range consists of 5 different threshold values. Averaging over these uncertainties yields a sufficient estimate for the accuracy $\Delta\eta$ of the method.
Uncertainties in the spectra and the phase speed were estimated as follows. The spectra result from averaging over a set of N sequences and therefore provide some statistical uncertainty, described by their standard deviation σ. Then, the statistical

uncertainty is the uncertainty of the mean

$$(\Delta\phi)_{stat} = \frac{\sigma}{\sqrt{N}} \ . \tag{5.49}$$

Furthermore, the uncertainty in the detected height $\Delta\eta$ contributes to the accuracy of the spectra. Detailed calculations for the propagation of uncertainty in Fourier transformed signals are supplied in appendix A. The theoretical uncertainty of a single spectrum ϕ_i depends on the length of the sequence, i.e. the number of data points M

$$(\Delta\phi)_{th,i} = \sqrt{\frac{2}{M}}\ \Delta\eta\ |\tilde{\eta}| \tag{5.50}$$

where $|\tilde{\eta}|$ is the absolute value of the Fourier transform of the sequence. Thus, the uncertainty of the power spectrum comprises

$$\Delta\phi = \sqrt{\left(\frac{\sigma}{\sqrt{N}}\right)^2 + \left(\frac{1}{N}\sum_{i=1}^{N}\left[(\Delta\phi)_{th,i}\right]^2\right)^2} \ . \tag{5.51}$$

In order to compute the phase speed, the derivatives in space and time direction of the height are used. Their uncertainty is approximated with help of the uncertainty of the symmetric difference quotient

$$\Delta f'(x_0) = \frac{f^{(3)}(x_0)}{6}h^2 \tag{5.52}$$

where h is the spacing between the data points [Burden and Faires, 2011, chap. 4]. To obtain a good estimate, it was considered satisfactory to approximate the third derivative with the mean of its absolute value, yielding

$$\Delta\phi_{\dot{\eta}} = \overline{\left(\left|\frac{\partial^3\eta}{\partial t^3}\right|\right)}\frac{h_t^2}{6} \tag{5.53}$$

$$\Delta\phi_s = \overline{\left(\left|\frac{\partial^3\eta}{\partial x^3}\right|\right)}\frac{h_x^2}{6} \ . \tag{5.54}$$

The spectra of the derivatives are ultimately divided as described in section 5.2. Consequently, their uncertainties influence the phase speed as follows

$$\Delta c = \frac{1}{2c}\sqrt{\left(\frac{\Delta\phi_{\dot{\eta}}}{\phi_s}\right)^2 + \left(\frac{\phi_{\dot{\eta}}}{\phi_s^2}\Delta\phi_s\right)^2} \ . \tag{5.55}$$

6. Results

This section presents the results of data evaluation with the algorithms described in section 5. Firstly, the extracted height is examined in section 6.1 and conclusions about general parameters of the wave fields, like maximum amplitude, significant wave height and mean square slope are drawn. All evaluated parameters are provided in table 2. In section 6.2 the frequency spectra of height and slope are shown and interpreted. The chapter ends with a discussion of the resulting dispersion relation in section 6.3. In this chapter exemplary plots are shown to illustrate the results. To be complete, the frequency spectra of height and slope, as well as the dispersion relations of the remaining data sets are supplied in appendix B.

6.1. Height Measurements

Figure 14 shows exemplary time series at 10 m/s wind speed for different paddle waves, i.e. mechanically generated waves. This form of visualization gives a good impression about the temporal behavior of the wave field. Additionally, a rough idea about the accuracy of the method can be gained, as the fitted height is overlaid on top of the images. A quantitative criterion for the quality of the height detection is provided in terms of the standard deviation (see section 5.4). For the data sets evaluated in this work, it was in the order of $\Delta\eta = 0.1\,\mathrm{pxl}$ which, with a scaling factor of $f_{cal} = 183\,\mu\mathrm{m/pxl}$, corresponds to $18.3\,\mu\mathrm{m}$ (see table 2).
As discussed in section 5.1, values with high standard deviation as well as points with strong deviation from the median are ignored in the detection process. Therefore, another beneficial quantity is the ratio ϵ of 'NaN's to all values (equation 5.45). This ratio is found to increase with wind speed (table 2). Partly, this is due to the implemented median filter, which only allows a certain steepness of the waves. The major cause though, are more frequently appearing dark regions in the images (see for example figure 11). This can result from bubbles, which can scatter the light, or may be caused by waves, that propagate between the side wall of the tank and the laser sheet and therefore mask the surface. At high wind speeds the presence of spray might be another cause and for steep slopes reflections of the laser beam can alter the lighting conditions as well.
For wind speeds of up to 10 m/s and without additional generated waves this is a minor issue, because the waves behave smoothly and a sufficient number of reliable data points is available for fitting (run 1-5, 8, 11). At higher wind speeds and with mechanically generated waves though, the waves have larger amplitudes and also break

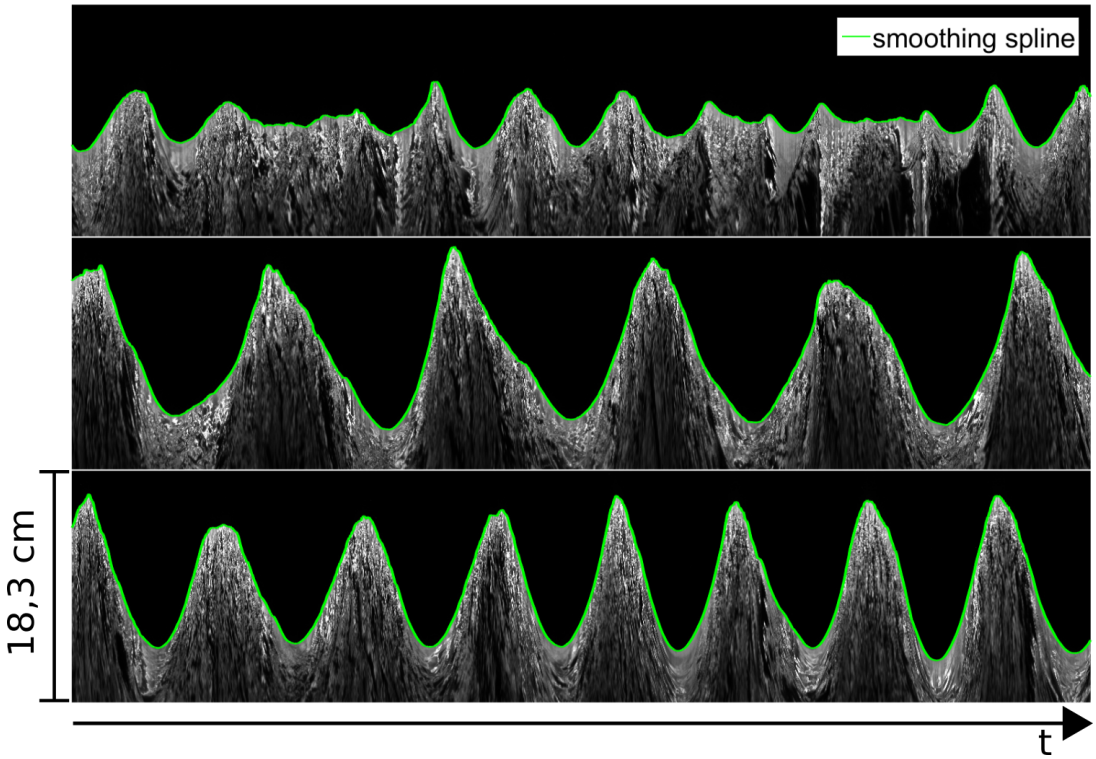

Figure 14: Time profile images for run 11 - 13. The time profile images show the column in the middle of the detection range as time advances from left to right in the image. Pure wind waves are shown at the top, paddle waves with 0.9 Hz in the middle and with 1.3 Hz at the bottom. The wind speed was 10 m/s and the sequences correspond to a measurement time of 6 s. The cubic smoothing spline fit is depicted as green line.

more often, which intensifies the occurrence of dark regions in the images. This can result in no, or even worse, faulty detection of the wave height, misguiding the subsequent data fitting. However, even at the highest wind speed and with mechanically generated waves of 1.3 Hz defective points have a very limited influence on the data set as a whole, as can be seen in figure 15.

Amongst others, the extracted data was used to calculate the maximum amplitudes in positive ($A_{max,+}$) and negative ($A_{max,-}$) direction with respect to the mean height. The results are presented in table 2. In addition to a general increase of amplitude with wind speed, the color scaling of the table indicates, that the highest surface elevation is obtained for generated waves with medium frequency. Similar observations can be

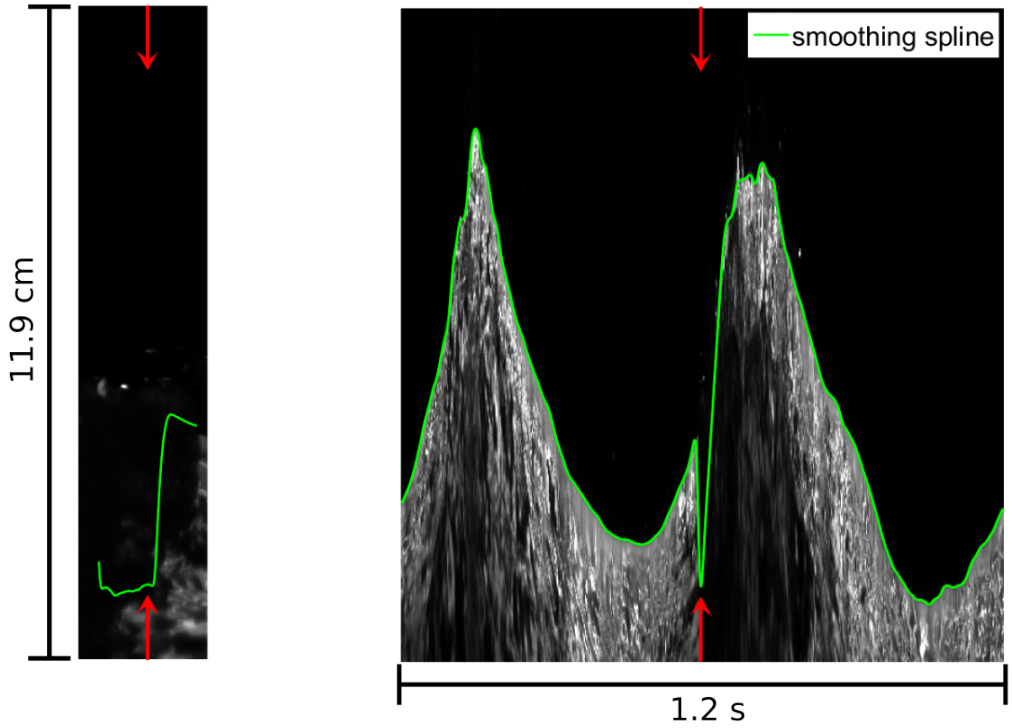

(a) Spatial Image

(b) Time profile image

Figure 15: Faulty detection of the height at 14 m/s wind speed and paddle waves with 1.3 Hz (run 18). In figure (a) an incorrect wave height is detected, because the actual surface appears not bright enough with respect to the determined threshold. However, the effect on the overall height is very limited as the time profile image in figure (b) shows. Corresponding columns are marked with red arrows.

run	wind [m/s]	paddle [Hz]	$A_{max,+}$ [mm]	$\Delta A_{max,+}$ [mm]	$A_{max,-}$ [mm]	$\Delta A_{max,-}$ [mm]	$A_{max,+}$ / $A_{max,-}$	H_s [mm]	ΔH_s [mm]	mss	Δmss	$\Delta\eta$ [mm]	ε
1	2,5	0	6,42	0,02	4,60	0,01	1,4	6,73	0,01	0,01438	0,00003	0,010	0,0001
2	3	0	9,55	0,03	6,86	0,02	1,4	10,27	0,02	0,01685	0,00005	0,013	0,0004
3	4	0	15,62	0,05	10,79	0,03	1,4	16,92	0,03	0,02062	0,00005	0,018	0,0018
4	5	0	20,9	0,2	14,27	0,07	1,5	23,3	0,1	0,0247	0,0002	0,015	0,0033
5	6	0	26,5	0,6	18,1	0,3	1,5	29,6	0,4	0,0318	0,0005	0,014	0,0011
6	6	0,9	50,6	0,2	52,8	0,5	1,0	123,5	0,9	0,043	0,001	0,012	0,0004
7	6	1,1	87,4	0,5	58,2	0,6	1,5	147,0	1,5	0,054	0,001	0,012	0,0005
8	6	1,3	80,9	0,7	50,3	0,6	1,6	119,1	0,8	0,088	0,003	0,018	0,0047
9	8	0	37,4	0,4	24,5	0,3	1,5	42,8	0,2	0,049	0,002	0,013	0,0015
10	8	0,9	87,1	1,1	51,3	0,8	1,7	134,2	2,0	0,054	0,004	0,015	0,0024
11	10	0	50,1	0,5	32,2	0,6	1,6	58,2	0,3	0,099	0,003	0,017	0,0046
12	10	0,9	92,5	1,4	67,7	0,8	1,4	160,9	2,1	0,105	0,002	0,017	0,0046
13	10	1,3	88,6	2,1	57,3	0,4	1,5	118,0	2,9	0,138	0,005	0,021	0,0105
14	12	0	64,7	0,7	41,5	0,9	1,6	75,3	0,6	0,160	0,004	0,021	0,0099
15	12	0,9	115,1	1,2	75,3	0,4	1,5	189,2	1,9	0,167	0,007	0,020	0,0091
16	14	0	76,6	0,4	47,3	0,5	1,6	92,9	0,6	0,157	0,005	0,023	0,0162
17	14	0,9	131,3	1,3	90,1	0,9	1,5	233,2	1,7	0,118	0,002	0,020	0,0092
18	14	1,3	109,9	1,9	68,5	0,3	1,6	129,9	2,3	0,21	0,02	0,02958	0,0257

Table 2: Evaluation of the fitted height. As indicated by the color scales, small wind speeds generally correspond to smaller amplitudes, a smaller significant wave height (H_s) and a smaller mean square slope in along-wind direction (mss). Moreover, fewer values are interpolated. If more than one data set was available to a set of conditions (run 5-18), the values of the sets were averaged and the uncertainties result from their standard deviation.

made from the time profiles in figure 14. Cause of this behavior is the limited steepness that waves can reach before breaking. Strongly simplified, the wave's steepness results from the ratio of amplitude to half a wave length, and consequently waves with smaller frequencies can grow higher before they break. Another interesting feature of the observed wave field reflects in the ratio of positive to negative maximum amplitude, provided in table 2. Here, significant non-linear behavior of the waves becomes apparent, as the maximum amplitude in positive direction is approximately 1.5 times as large as the amplitude in negative direction for all runs. This implies, that even at the lowest wind speeds, the waves show the typical sharpened crests and flatted troughs of Stokes waves, which is also prominent in figure 14.
The significant wave height reveals information about the statistical distribution of the waves, as it describes the mean height from crest to trough of the highest third of the waves [Holthuijsen, 2007]. The computed values result from equation 5.47. As illustrated in table 2, the over all behavior of the significant wave height mirrors that of the maximum amplitudes. It can be seen, that values for mechanically generated waves with 1.3 Hz are smaller than for 0.9 Hz, and do not vary much with the wind speed. This indicates, that waves with this frequency already break at a wind speed of 6 m/s. Note, that the corresponding wavelength of a deep water gravity wave with small amplitude and 1.3 Hz is approximately 0.9 m.
Further, the mean square slope in along-wind direction was calculated from the data. As it is a measure for the roughness of the surface, its increase with wind speed matches the expectations. It is noted, that values between pure wind waves and additional generated waves with 0.9 Hz differ only slightly, but when wave breaking occurs at 1.3 Hz, the roughness of the surface is increased.

6.2. Wave Spectra

Within the script for data evaluation frequency spectra of height, slope as well as the time derivative were computed. Due to the reasons discussed at the end of section 5.2, it was decided to use the fitted data from the cubic smoothing spline as input. The presented spectra result from an ensemble average of one-minute time segments (see section 5.2) and subsequent frequency averaging. Regions with uncertainties of more than 10% are pictured in pale color.
Figure 16 shows the spectra of the wave height for exemplary wind speeds. It can be seen that the general amplitude increases with wind speed, which matches the expectations, as higher wind speeds correspond to an enhanced exchange of momentum and thus to a higher energy of the wave field. Furthermore, for purely wind generated

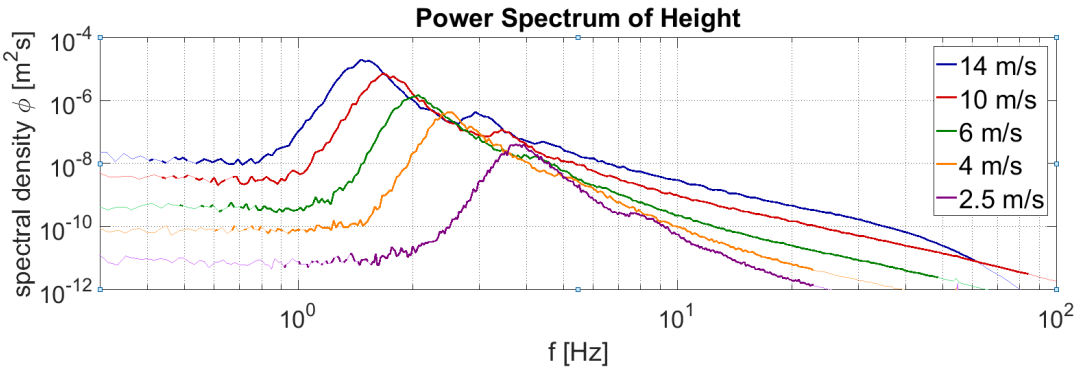

(a) Pure wind waves

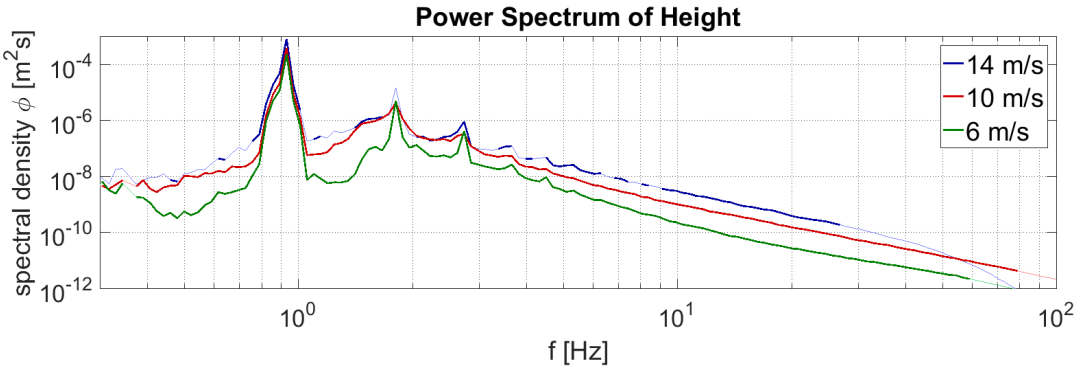

(b) Mechanically generated waves with 0.9 Hz

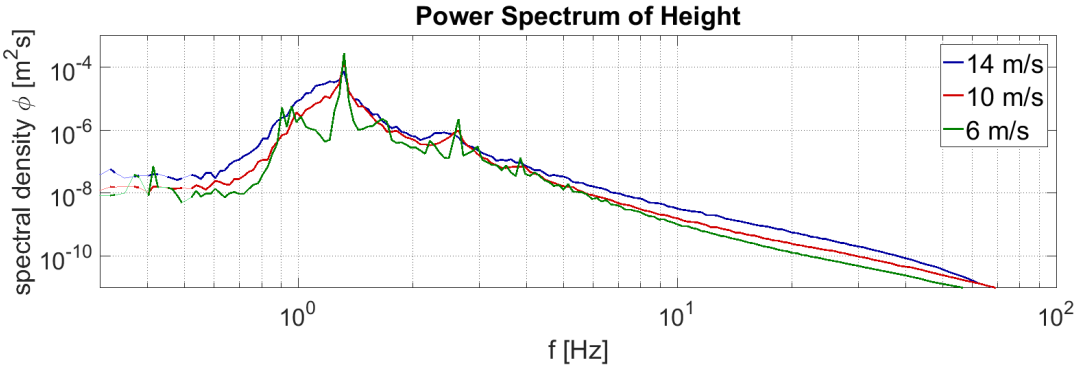

(c) Mechanically generated waves with 1.3 Hz

Figure 16: Frequency power spectra of the wave height for run 1, 3, 5, 11, 16 (top), 6, 12, 17 (middle) and 8, 13, 18 (bottom). With increasing wind speed the energy in the wave field enlarges, and the dominant waves become longer, if the waves are purely wind generated (figure (a)). The frequency of mechanically generated dominant waves is found to be independent of the wind speed (figure (b) and (c)). A sharp cut off for 14 m/s at approximately 80 Hz is observed. Potentially, this results from difficulties in the detection process, as strong turbulence and spray are present at this condition.

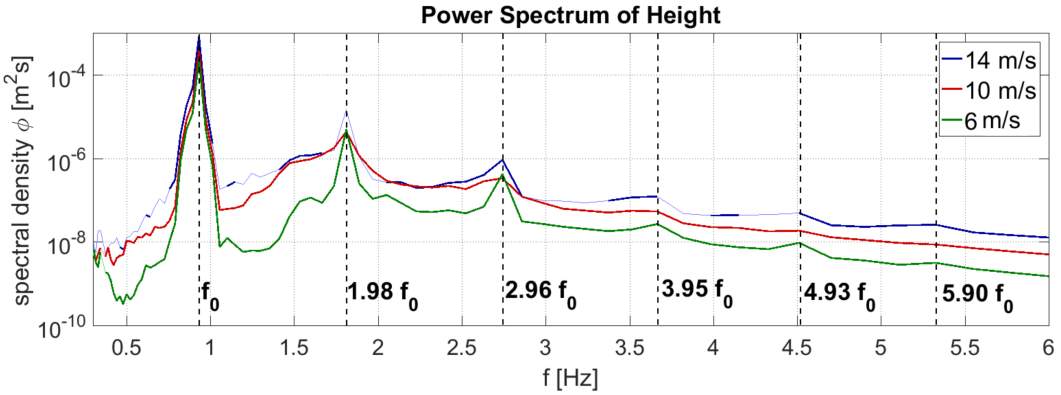

Figure 17: Frequency power spectra for mechanically generated waves with 0.9 Hz (run 6, 12, 17). For all wind speeds the peak is at $f_0 \approx 0.917$ Hz and local maxima are approximately found at $2f_0$, $3f_0$, $4f_0$ and $5f_0$. This indicates the presence of a fundamental wave with bound harmonics.

waves the peaks of the spectra move to smaller frequencies, indicating that long waves prevail at higher wind speeds. Then again, for mechanically generated waves the peaks remain at fixed frequencies, independent of the wind speed. This shows, that the wind has no significant impact on the frequency of the generated fundamental wave. At a wind speed of 14 m/s a sharp cut off is observed at about 80 Hz for pure wind waves as well as mechanically generated waves. The same effect is found in the slope spectra (see figure 19). It is possible, that this originates from difficulties in the height detection, rather than from the actual wave field. As the waves feature strong turbulent behavior and a lot of spray is present at these conditions, the detection of small scale waves is potentially affected. This could account for an artificial cut off at higher frequencies.

As already indicated by the amplitude measurements in 6.1, the wave field features significant non-linear behavior, which also mirrors in the spectra. The wave profile of non-linear Stokes waves is no longer sinusoidal, but rather arises from superposition of the fundamental wave with its harmonics [Kundu and Cohen, 2008, chap. 7.13]. The harmonics, i.e. bound waves, are therefore expected to appear in the spectrum at integer multiples of the frequency of the fundamental wave. This phenomenon is observed in all computed spectra, but is revealed particularly well for the case of additional mechanically generated waves. In figure 17 an excerpt of the spectra for waves with 0.9 Hz is shown. For all wind speeds the peak was identified at $f_0 \approx 0.917$ Hz reflecting the fundamental wave generated with 0.9 Hz. Besides the peak,

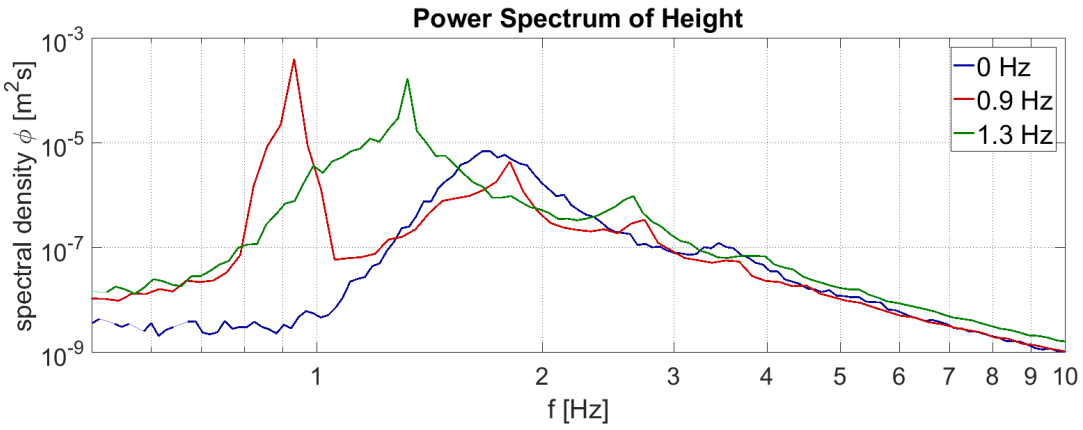

Figure 18: Excerpt of the frequency power spectra at a wind speed of 10 m/s (run 11-13). The presence of mechanically generated waves damps all frequencies but the harmonics.

local maxima are apparent at multiples of f_0, corresponding to the bound harmonics. Complementary to the influence of wind, the effects of mechanically generated waves shall now be examined more closely. In figure 18 different spectra at a wind speed of 10 m/s are presented. It is observed, that, if paddle waves are generated, wave frequencies other than the fundamental and its harmonics are damped. This is already indicated by the time profile images in figure 14. For pure wind waves a variety of amplitudes and frequencies is present, whereas the wave fields with mechanically generated waves appear relatively uniform. This becomes yet more evident, when looking at the spectra in figure 18. For generated waves the energy density is sharply peaked at the fundamental frequency and its harmonics, whereas a rather smooth distribution is observed for pure wind waves.

Further, the evaluated data allows an analysis of the slope spectra of the observed wave fields. Exemplary results for pure wind waves and mechanically generated waves at different wind speeds are depicted in figure 19. The previously described effects of non-linear waves are present in the slope spectra as well. In addition, a secondary bump becomes apparent at frequencies between 30 Hz and 100 Hz. Similar observations for pure wind waves were made by Jähne [1989], where it is stated, that the bump arises from additional capillary waves, directly generated by instabilities of the dominant gravity waves.

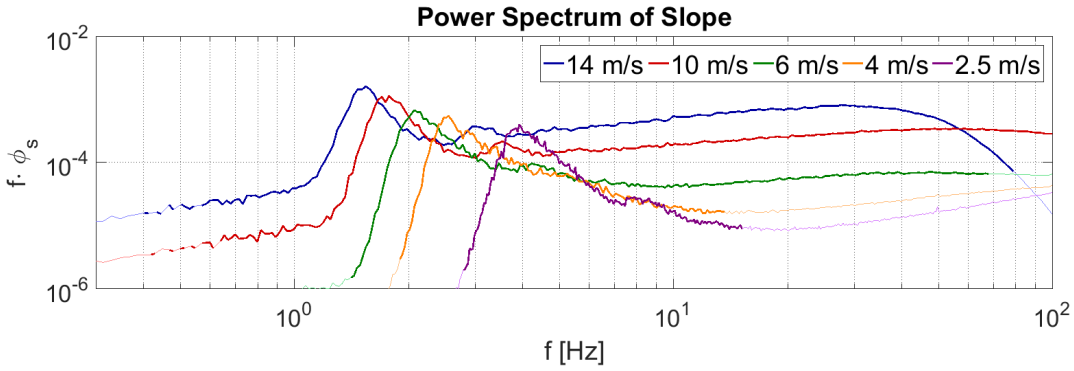

(a) Pure wind waves

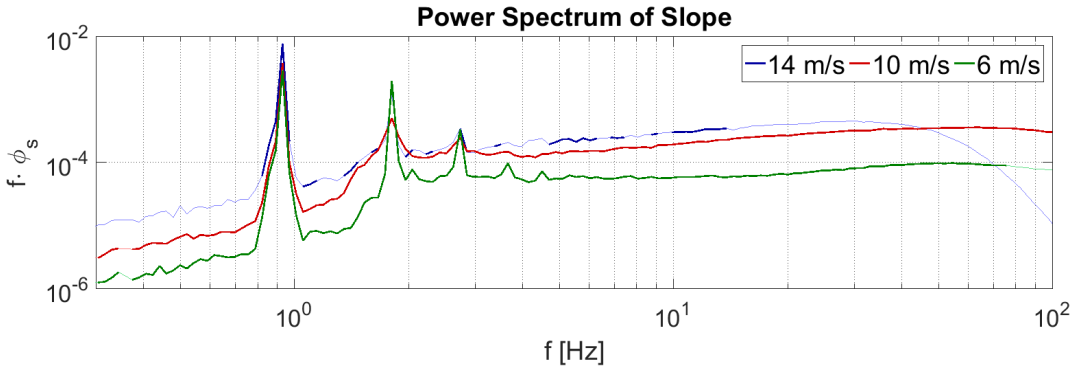

(b) Mechanically generated waves with 0.9 Hz

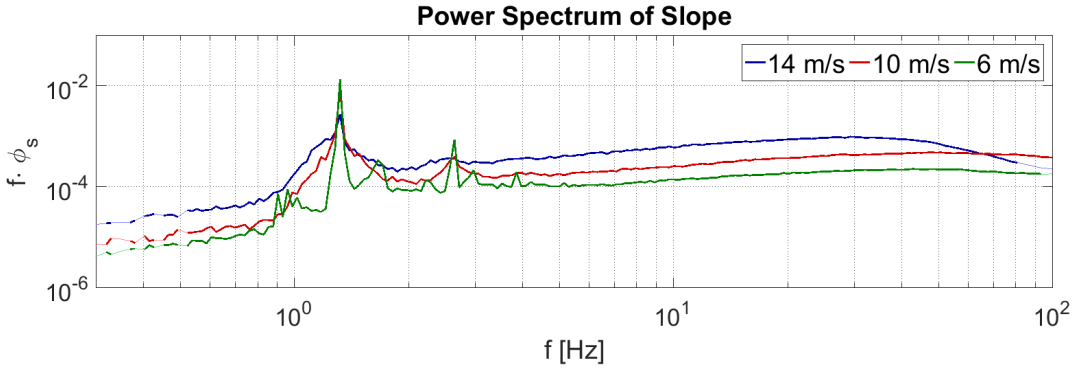

(c) Mechanically generated waves with 1.3 Hz

Figure 19: Frequency power spectra of the slope for run 1, 3, 5, 11, 16 (top), 6, 12, 17 (middle) and 8, 13, 18 (bottom). For scaling purposes the spectral density is multiplied with the frequency. Secondary bumps are apparent in regions of 30 Hz - 100 Hz.

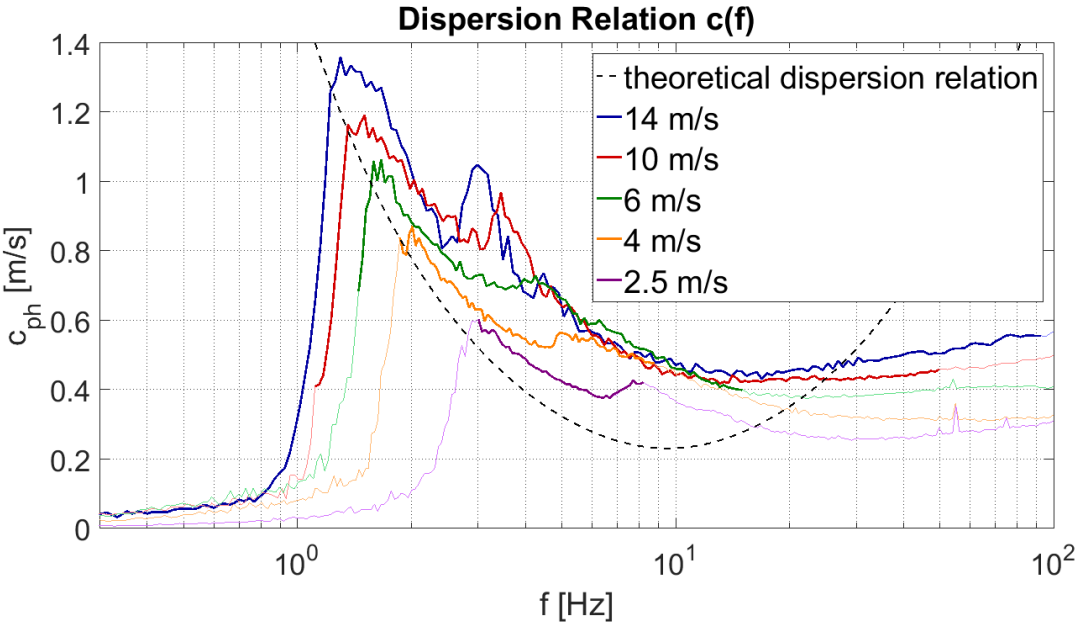

Figure 20: Dispersion relation for purely wind generated wave fields (run 1, 3, 5, 11, 16). The dominant waves have phase speeds close to the theoretical dispersion relation, but for higher frequencies non-linear behavior causes a significant deviation.

6.3. Phase Speed

Lastly, the dispersion relation was computed for all data sets. The results are presented in this section. Again, regions with uncertainties of more that 10% are colored pale in the plots and frequency averaging was performed, such that the data points are equally spaced on a logarithmic scale.

In figure 20 the phase speeds for purely wind generated wave fields are shown. The dashed line marks the theoretical dispersion relation for small amplitude waves (equation 2.11). Over all, the computed phase speeds are in excess of the theoretical values for frequencies above the peak. This is a typical observation for non-linear wave fields, as the effects of finite amplitudes can account for an increase in phase speed. On the one hand a finite amplitude leads to a decrease of the wavenumber for a given frequency. Commonly, this is referred to as amplitude dispersion, and can cause an increase in phase speed of up to 10% [Donelan et al., 1985]. On the other hand, the previously mentioned bound waves are a consequence of finite amplitudes. Other than

the fundamental wave, the harmonics do not follow the theoretical dispersion relation [Komen, 1980]. This can be seen from the secondary peak in figure 20, but becomes even more apparent when looking at the phase speeds of additional mechanically generated waves shown in figure 21. The phase speeds of the fundamental waves are, considering effects of amplitude dispersion, in good accordance with the theoretical value. On the contrary, velocities for higher harmonics are significantly enlarged. Since the harmonics are bound to the fundamental waves, it is expected that they propagate with the same speed. At high wind speeds ($\geq 10\,\mathrm{m/s}$) this is observed indeed, but the effect weakens with higher order of the harmonic and decreasing wind.

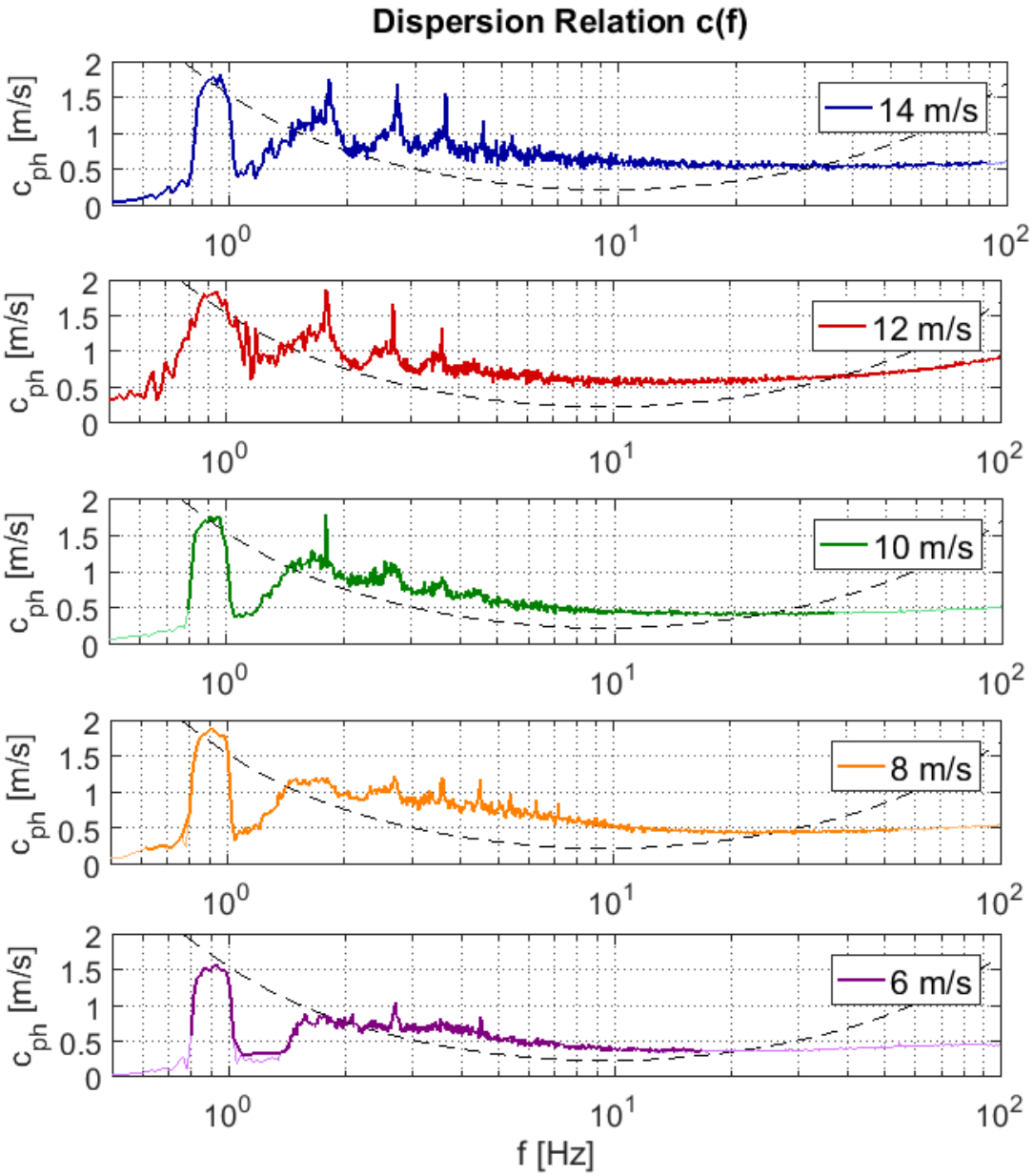

Figure 21: Dispersion relation for mechanically generated waves of 0.9 Hz (run 6, 10, 12, 15, 17). The fundamental waves have phase speeds close to the theoretical dispersion relation, whereas higher harmonics show significantly enlarged phase speeds.

7. Conclusions and Outlook

Height Detection

A reliable detection of the shape of the water surface is crucial for a detailed description of the wave field. Within this work, a measurement technique based on laser-induced fluorescence was used to visualize the surface position. This technique was previously applied by Horn [2013], and has recently been extended from a laser point to a laser sheet. Therefore, it is now possible to measure both, spatial and temporal information about the height. In order to process the surface profile images, an algorithm was designed, which is capable of detecting the surface position and applies subsequent spatio-temporal smooth fitting (figure 13). If the images feature a sharp difference in gray values between water and air, the algorithm provides reliable results and reaches an accuracy of about 18 μm. However, at higher wind speeds and when additional waves are generated, dark regions arise more frequently at the interface in the images (section 6.1). To identify these areas, the detected height values undergo subsequent filtering, where faulty detected positions are discarded and interpolated. Again, the algorithm performs well, if the regions are sufficiently small and an overall smooth behavior of the wave field is present (section 5.2). This is usually the case for pure wind waves and wind speeds of up to 10 m/s. Then again, if dark regions are dominant and if faulty detection is not captured by the filtering, defective values of the surface position can occur (figure 15). As a consequence, the individual height detection becomes less precise at high wind speeds and if additional waves are generated, but through statistics, the characteristics of the wave field are still well identified (see section 6.1).

Wave Spectra

Within the script for data evaluation, frequency spectra of height, slope and time derivative were computed. For all conditions the phenomenon of bound harmonics was observed, but it is particularly pronounced, if the waves are generated mechanically, because then other wavelengths are damped (section 6.2). The slope spectra show a secondary bump, which corresponds to the observations made by Jähne [1989]. This indicates the generation of additional capillary waves through instabilities in the dominant gravity waves (section 6.2). At a wind speed of 14 m/s a sharp cut off at approximately 80 Hz is observed. It is possible, that this arises from difficulties in the detection process, rather than being an actual feature of the wave field. This could be investigated by checking the results against the ones obtained from the wave wires, as simultaneous measurements were made by our local partner Dr. Guillemette Caulliez from MIO, Marseille.

Phase Speed

Lastly, the dispersion relation was computed from the frequency spectra of slope and time derivative. Again, non-linear features of the wave field were observed for all conditions. The bound harmonics were found to propagate with the same speed as the fundamental wave, which matches the expectations. This effect weakens with decreasing wind, though (figure 21). Generally, the computed phase speed is slightly larger than predicted by the theory for small amplitude waves. This can be explained through the phenomenon of amplitude dispersion, which can account for an increase of the phase speed of up to 10% (section 6.3).

Outlook

The developed algorithm is capable of extracting the spatio-temporal surface position from large sets of surface profile images. For sufficiently calm behavior of the wave field, the detection is reliable and accurate. In order to achieve the same accuracy at high wind speeds and with mechanically generated waves, measures against the occurrence of dark regions in the images have to be realized. As discussed in section 6.1, waves between tank wall and laser sheet can mask the observed surface position. This could be prevented, by placing the camera further above the water surface in future experiments, which would enlarge the angle under which the surface is observed. Then, waves in the foreground are less likely to overlap with the field of view. To correct for a reduced intensity due to scattering of the light, e.g. by bubbles, adjusted gray value thresholds could be computed in the affected images, instead of using the fixed values determined from a series of images in the beginning. This could reduce faulty detection at the expense of a higher computational cost. Alternatively, a different approach in filtering the images could be considered. Caulliez, for example, applies an algorithm based on the Canny edge detector to extract the wave profiles from the images [Caulliez, 2013].

Moreover, the high flexibility of the implemented P-Spline method can be exploited further. Within the framework of this thesis, only a small parameter range was tested, to determine appropriate settings for smooth fitting. Further investigation on different degrees of splines and orders of the penalties can be made, to optimize the fitting properties.

As the wave height was also measured with wave wires 3 m behind the measurement section by our local partner Dr. Guillemette Caulliez, a comparison of the results would be interesting. Furthermore, the computed mean square slope in along wind direction remains to be checked against the results from the laser slope gauge, which

was installed at the same fetch.
The image processing algorithms developed in this work are generally applicable to all images with a sharp gradient between water surface and air. Therefore, the algorithm and the script for data evaluation can be readily used as a tool in future experiments with a set up similar to the one in figure 6.

References

G. Balschbach. *Untersuchungen statistischer und geometrischer Eigenschaften von Windwellen und ihrerWechselwirkungen mit der wasserseitigen Grenzschicht*. Dissertation, Ruperto-Carola University of Heidelberg, 2000. URL `http://katalog.ub.uni-heidelberg.de/titel/64232452`.

G. Betta, C. Liguori, and A. Pietrosanto. Propagation of uncertainty in a discrete Fourier transform algorithm. *Measurement*, 27(4):231–239, 2000. ISSN 02632241. doi: 10.1016/S0263-2241(99)00068-8.

R. L. Burden and J. D. Faires. *Numerical Analysis*. 2011. ISBN 978-0-538-73564-3.

G. Caulliez. Dissipation regimes for short wind waves. *Journal of Geophysical Research: Oceans*, 118(2):672–684, 2013. ISSN 21699291. doi: 10.1029/2012JC008402.

D. J. Chen. *Designing Wave-measuring Instruments*. Master thesis, Massachusetts Institute of Technology, 1994.

C. De Boor. *A Practical Guide to Splines*. Springer, New York, 6. print edition, 1978. ISBN 0-387-90356-9. URL `http://katalog.ub.uni-heidelberg.de/titel/3006343`.

M. A. Donelan, J. Hamilton, and W. H. Hui. Directional Spectra of Wind-Generated Waves. *Philos. Trans. Roy. Soc. London*, A315:509–562, 1985. ISSN 1364-503X. doi: 10.1098/rsta.1948.0007.

P. H. C. Eilers and B. D. Marx. Flexible Smoothing with B-splines and Penalties. *Statistical Science*, 11(2):89–121, 1996. doi: 10.1214/ss/1038425655.

P. H. C. Eilers, I. D. Currie, and M. Durbán. Fast and compact smoothing on large multidimensional grids. *Computational Statistics & Data Analysis*, 50:61–76, 2006. doi: 10.1016/j.csda.2004.07.008.

D. Eisenhauer. *Aufbau eines Messsystems zur Amplitudenmessung von Schwerewellen im Aeolotron*. Bachelor thesis, Ruperto-Carola University of Heidelberg, 2011.

L. H. Holthuijsen. *Waves in Oceanic And Coastal Waters*. Cambridge University Press, 2007. ISBN 978-0521860284. doi: 10.1002/qj.324.

J. Horn. *Hochaufgelöste optische Wellenhöhenmessung am Aeolotron mit Laser-induzierter Fluoreszenz*. Bachelor thesis, Ruperto-Carola University of Heidelberg, Heidelberg, 2013.

IPCC. Climate Change 2014: Mitigation of Climate Change. *Fifth Assessment Report of the Intergovernmental Panel on Climate Change*, 2014.

B. Jähne. Optical water waves measuring techniques. In *1st International Symposium on Gas Transfer at Water Surfaces*, Cornell University, Ithaca, New York, 1983. doi: 10.5281/zenodo.14008.

B. Jähne. Energy balance in small-scale waves - an experimental approach using optical slope measuring technique and image processing. In G. J. Komen and W. Oost, editors, *Radar Scattering from Modulated Wind Waves*, pages 105–120. Kluwer, Boston, 1989. ISBN 9789401075374. doi: 10.1007/978-94-009-2309-6.

B. Jähne. *Digitale Bildverarbeitung und Bildgewinnung*. Springer, 7 edition, 2012. ISBN 978-3-642-04951-4. doi: 10.1007/978-3-642-04952-1.

D. Kiefhaber. *Development of a Reflective Stereo Slope Gauge for the measurement of ocean surface wave slope statistics*. Diploma thesis, Ruperto-Carola University of Heidelberg, 2010. URL `http://katalog.ub.uni-heidelberg.de/titel/67125364`.

G. Komen. Nonlinear Contributions to the Frequency Spectrum of Wind-Generated Water Waves. *J. phys. Oceanogr.*, 5:779–790, 1980. doi: 10.1175/1520-0485(1980)010⟨0779:NCTTFS⟩2.0.CO;2.

C. Kräuter. *Visualization of air-water gas exchange*. Dissertation, Ruperto-Carola University of Heidelberg, 2015. URL `http://katalog.ub.uni-heidelberg.de/titel/67809534`.

P. K. Kundu and I. M. Cohen. *Fluid Mechanics*. 2008. ISBN 978-0-08-055583-6. URL `http://proquest.tech.safaribooksonline.de/9780123737359`.

W. Laas. Photographische Messung der Meereswellen. *Ztschr Ver. Dtsch Ingenieure*, 49, 1905.

N. Otsu. A threshold selection method from gray-level histograms. *IEEE Transactions on Systems, Man, and Cybernetics*, 9(1):62–66, 1979. doi: 10.1109/TSMC.1979.4310076.

B. Peter. *Entwicklung eines Messsystems zur Amplitudenmessung von Wasserwellen im Aeolotron*. Bachelor thesis, Ruperto-Carola University of Heidelberg, 2015.

O. M. Phillips. *The Dynamics of the Upper Ocean*. Cambridge University Press, 2 edition, 1977. ISBN 0-521-29801-6.

M. Raffel, C. E. Willert, and J. Kompenhans. *Particle Image Velocimetry*. Springer, 1998. ISBN 3-540-63683-8.

C. H. Reinsch. *Smoothing by Spline Functions*. 1967. doi: 10.1007/BF02162161.

R. Rocholz. *Spatio-Temporal Measurement of Short Wind-Driven Water Waves*. Dissertation, Ruperto-Carola University of Heidelberg, 2008. URL `http://katalog.ub.uni-heidelberg.de/titel/66646691`.

I. J. Schoenberg. Spline Functions and the Problem of Graduation. *Proceedings of the National Academy of Sciences of the United States of America*, 52(4):947–950, 1964. ISSN 0027-8424. doi: 10.1073/pnas.52.4.947.

S. Waas and B. Jähne. Combined slope-height measurements of short wind waves: First results from Field and laboratory measurements, in Optics of the Air-Sea Interface: Theory and Measurements. *SPIE Proc.*, 1749:295–306, 1992. URL `stacks.iop.org/MST/16/1937`.

R. Wanninkhof, W. E. Asher, D. T. Ho, C. Sweeney, and W. R. McGillis. Advances in quantifying air-sea gas exchange and environmental forcing. *Annual review of marine science*, 1:213–244, 2009. ISSN 1941-1405. doi: 10.1146/annurev.marine.010908.163742.

E. T. Whittaker. On a New Method of Graduation. *Proceedings of the Edinburgh Mathematical Society*, 41:63–75, 1923. ISSN 1464-3839. doi: 10.1017/S001309150000359X.

A. Error Calculations for the DFT

The subsequent calculations follow the concepts for error propagation presented in [Betta et al., 2000].
Consider the discrete Fourier transform of a noisy signal $f + \Delta f$. For convenience, we express the Fourier transform in terms of its real and imaginary part

$$\tilde{f}_{\tilde{n}} = \frac{1}{N}\left(R(\tilde{n}) - iI(\tilde{n})\right) \tag{1.56}$$

with

$$R(\tilde{n}) = \sum_{n=0}^{N-1} f_n \cos\left(\frac{2\pi n\tilde{n}}{N}\right) \tag{1.57}$$

$$I(\tilde{n}) = \sum_{n=0}^{N-1} f_n \sin\left(\frac{2\pi n\tilde{n}}{N}\right) \ . \tag{1.58}$$

Supposing that $\Delta f_n = \Delta f$ it follows that

$$(\Delta R)^2 = \sum_{n=0}^{N-1}\left(\frac{\partial R}{\partial f_n}\Delta f_n\right)^2 = (\Delta f)^2 \sum_{n=0}^{N-1}\cos^2\left(\frac{2\pi n\tilde{n}}{N}\right) \tag{1.59}$$

$$(\Delta I)^2 = \sum_{n=0}^{N-1}\left(\frac{\partial I}{\partial f_n}\Delta f_n\right)^2 = (\Delta f)^2 \sum_{n=0}^{N-1}\sin^2\left(\frac{2\pi n\tilde{n}}{N}\right) \tag{1.60}$$

$$(\Delta(R,I))^2 = \sum_{n=0}^{N-1}\frac{\partial R}{\partial f_n}\frac{\partial I}{\partial f_n}(\Delta f_n)^2 = (\Delta f)^2 \sum_{n=0}^{N-1}\cos\left(\frac{2\pi n\tilde{n}}{N}\right)\sin\left(\frac{2\pi n\tilde{n}}{N}\right) \ . \tag{1.61}$$

As $\sum \cos(x)\sin(x) = 0$ for all x it holds that

$$(\Delta(R,I))^2 = 0 \ . \tag{1.62}$$

Using:

$$\sum_{n=0}^{N-1}\cos^2\left(\frac{2\pi n\tilde{n}}{N}\right) = \sum_{n=0}^{N-1}\sin^2\left(\frac{2\pi n\tilde{n}}{N}\right) = \frac{N}{2} \quad \text{for} \quad n > 0 \tag{1.63}$$

it further simplifies for $n > 0$:

$$(\Delta R)^2 = \frac{N}{2}(\Delta f)^2 \tag{1.64}$$

$$(\Delta I)^2 = \frac{N}{2}(\Delta f)^2 \ . \tag{1.65}$$

With the error of the Fourier transform derived, we now determine the error of the module M, given by:

$$M = \frac{1}{N}\sqrt{R^2 + I^2} \ . \tag{1.66}$$

Applying the common laws of error propagation, the error is obtained

$$(\Delta M)^2 = \frac{1}{N^4 M^2}\left((R\Delta R)^2 + (I\Delta I)^2 + 2RI\Delta(R,I)\right) \tag{1.67}$$

$$= \frac{1}{2N}(\Delta f)^2 \quad \text{for} \quad n > 0 \ . \tag{1.68}$$

Lastly, we examine the error of the squared module according to the power spectrum:

$$(\Delta M^2) = 2M\Delta M = M\sqrt{\frac{2}{N}}\Delta f \ . \tag{1.69}$$

This indicates, that the uncertainty of the power spectrum depends on the length N of the signal. Furthermore, it states proportional scaling of the error to the module.

B. Complementary Frequency Spectra and Dispersion Relations

For completeness, complementary frequency spectra of height and slope and the dispersion relations of all evaluated data sets are supplied in this section. In the plots regions with uncertainties of more that 10% are painted in pale color and frequency averaging was performed, such that the data points are equally spaced on a logarithmic scale. Accordingly to section 6.2, the slope spectra are multiplied with the frequency for representation.

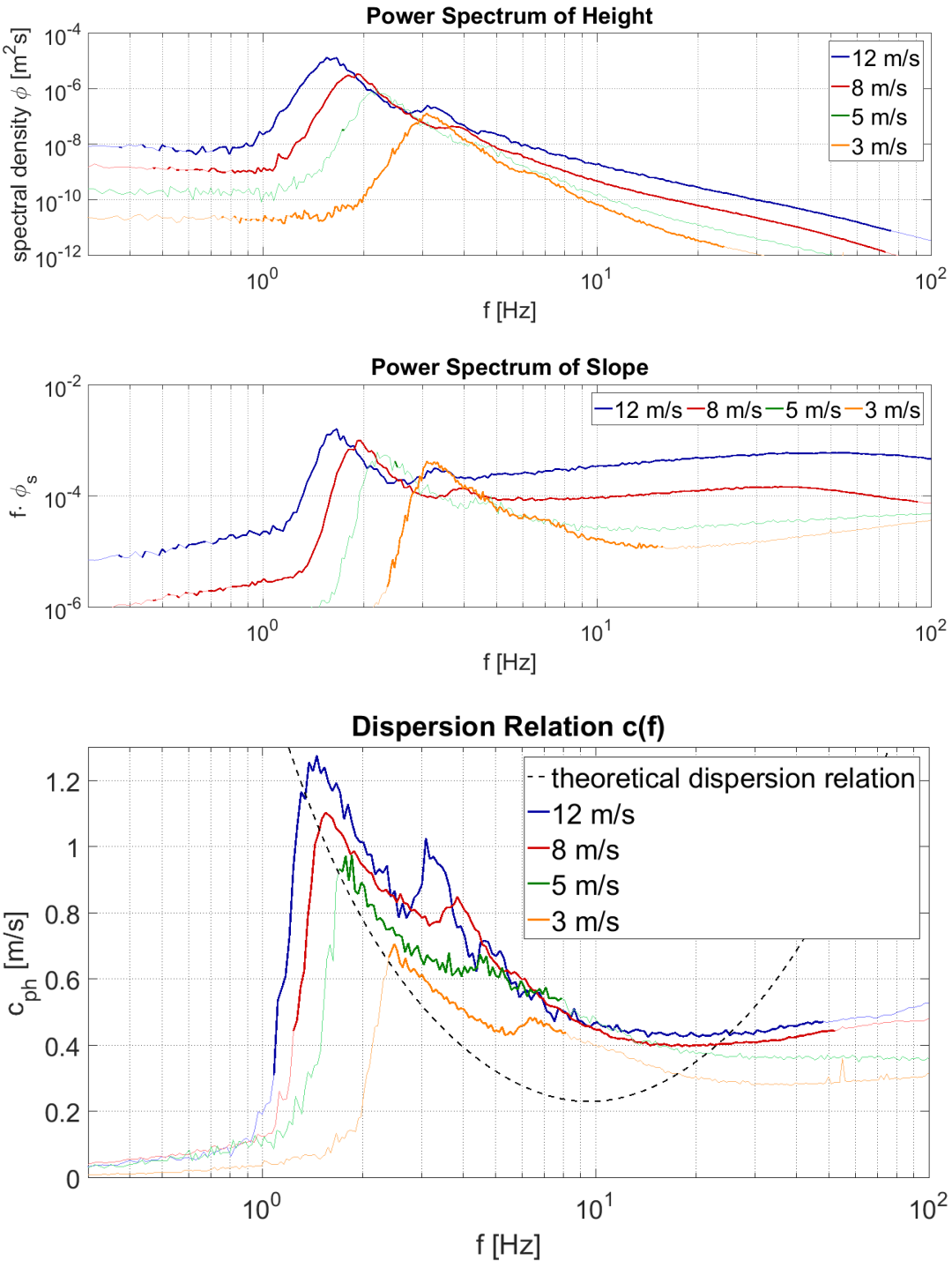

Figure 22: Frequency spectra and dispersion relations for pure wind waves at varying wind speeds (run 2, 4, 9, 14).

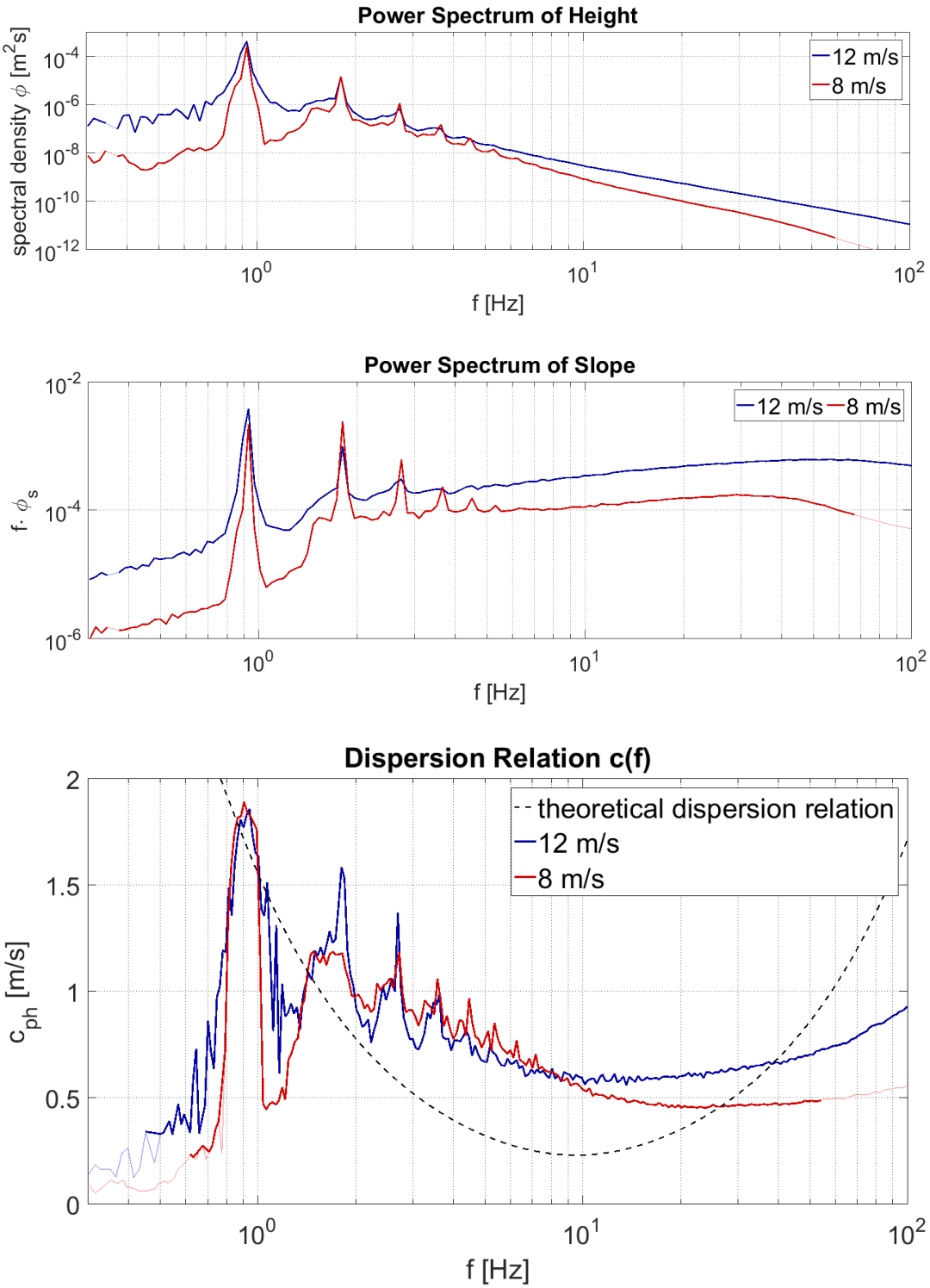

Figure 23: Frequency spectra and dispersion relations for additional mechanically generated waves with 0.9 Hz at varying wind speeds (run 10, 15).

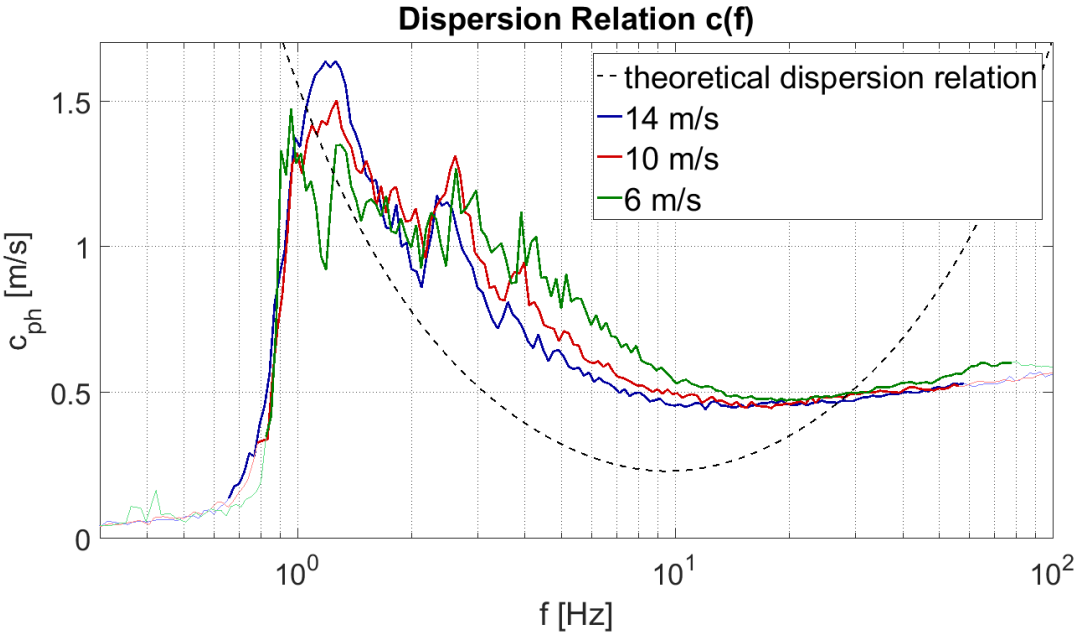

Figure 24: Dispersion relations for run 8, 13, 18, i.e. additional paddle waves with 1.3 Hz.